Collective modes in liquid binary alloys. An *ab initio* molecular dynamics study of the LiMg and LiBa alloys

2005 J. Phys.: Condens. Matter 17 1429

(http://iopscience.iop.org/0953-8984/17/10/002)

INSTITUTE OF PHYSICS PUBLISHING JOURNAL OF PHYSICS: CONDENSED MATTER

J. Phys.: Condens. Matter **17** (2005) 1429–1456 doi:10.1088/0953-8984/17/10/002

Collective modes in liquid binary alloys. An *ab initio* molecular dynamics study of the LiMg and LiBa alloys

D J González[1], L E González[1], J M López[1] and M J Stott[2]

[1] Departamento de Física Teórica, Universidad de Valladolid, 47011 Valladolid, Spain
[2] Department of Physics, Queen's University, Kingston, ON, K7L 3N6, Canada

Received 12 January 2005
Published 25 February 2005
Online at stacks.iop.org/JPhysCM/17/1429

Abstract

We report a study on several structural and dynamical properties of the liquid Li–Mg and Li–Ba alloys. The study has been carried out by means of the orbital free *ab initio* molecular dynamics method, combined with local ionic pseudopotentials constructed within the same framework. The results show good agreement with the available experimental data, accounting fairly well for the different ordering tendencies exhibited by these alloys. We analyse the dependence of the longitudinal and transverse collective modes on the concentration and the mass ratio of the alloy, with the latter ranging from $m_{\mathrm{Mg}}/m_{\mathrm{Li}} \approx 3$ to $m_{\mathrm{Ba}}/m_{\mathrm{Li}} \approx 20$.

1. Introduction

Ab initio molecular dynamics (AIMD) methods have become a usual technique in the study of the thermodynamic, structural and dynamical properties of liquid systems. Most applications of the AIMD methods are based on the density functional theory (DFT) [1, 2] which, for given nuclear positions, yields the ground state electronic energy of a collection of atoms as well as the forces on the nuclei. However, the AIMD methods that use the Kohn–Sham (KS) orbital representation of DFT (KS-AIMD methods) impose high computational demands, limiting the sample sizes and the simulation times; in fact, previous studies of bulk liquid metals and alloys [3–5] have used around one hundred atoms and simulation times between 2 and 5 ps. These limitations are partly overcome by the so-called orbital free *ab initio* molecular dynamics (OF-AIMD) method, which by resorting to the Hohenberg–Kohn (HK) representation of the DFT, eliminates the electronic orbitals of the KS formulation and provides a simulation method which allows simulations of much larger samples and for long times.

The study of the thermodynamic and structural properties of liquid metallic binary alloys has already produced much experimental and theoretical work which, however, is much more scarce when it comes to the dynamic properties. Nonetheless, the last twenty years have witnessed an increasing effort which was stimulated by a MD study of liquid Na–K [6], followed by a MD simulation of liquid Li_4Pb [7] where a new, high frequency mode,

supported by the Li atoms only (the so-called 'fast sound') was found. Subsequently, several theoretical calculations [8–13], computer simulations [14–16] and experiments [15, 17–19] have investigated the existence and properties of the collective excitations in liquid binary systems. On the theoretical side the application of the kinetic theory for a model binary mixture of hard spheres, the revised Enskog theory (RET) [8, 9], and the recent generalized collective model (GCM) approach [10] have given useful insights into the nature of the collective excitations. For binary systems with disparate masses, two main branches (low and high frequency ones) of collective excitations have been found to contribute to the longitudinal dynamics, although its origin is still unclear. On the other hand, the transverse dynamics has been much less investigated, mainly because it is not visible in scattering experiments and only the MD simulations can provide information about the transverse excitations. The recent application of the GCM approach, which combines MD simulations with the memory function formalism, to binary Lennard-Jones fluids and liquid alloys [10] has shown the existence of transverse optic modes, which arise in connection with concentration fluctuations.

This paper reports an AIMD study on the structural and dynamical properties of two Li-based liquid alloys, namely, $Li_{1-x}Mg_x$ and $Li_{1-x}Ba_x$. They have usually been considered as simple liquid alloys where the nearly free-electron theory should provide a reliable qualitative description of several structural and thermodynamic properties. On the experimental side, these alloys have been investigated by means of neutron scattering (NS) experiments by Ruppersberg and co-workers [20, 21]. Those experiments were performed within the context of a wider research programme aimed at analysing the total static structure factor, $S_T(q)$, of simple liquid binary alloys as the size mismatch between both components is increased. Within this program, NS experiments were performed on liquid binary alloys of Li with Mg, Ca, Sr and Ba, for which the ratios of the molar volumes of the pure components at their melting temperature are 1.16, 2.19, 2.61 and 3.06 respectively. The use of the ^{7}Li isotope, which has a negative neutron scattering length, meant that for a specific concentration of each alloy (the so-called 'zero-alloy' concentration), $S_T(q)$ reduces to the concentration–concentration partial structure factor, $S_T(q) = S_{CC}(q)/x_{Li}(1 - x_{Li})$, where x_{Li} is the Li concentration. This is very important as $S_{CC}(q)$ embodies most information concerning the ordering properties of the binary alloy which therefore can be obtained, at the 'zero-alloy' composition, from a single-neutron-scattering experiment.

The paper is organized as follows. In section 2 we briefly describe the theory used in the OF-AIMD simulations, and provide some details concerning the electronic kinetic energy functional and the local pseudopotential characterizing the electron–ion interaction. Sections 3 and 4 report the *ab initio* simulation results for the static and dynamic properties of the Li–Mg and Li–Ba liquid alloys at several concentrations. Finally, we sum up and discuss the results.

2. Theory

A simple liquid metallic alloy, A_xB_{1-x}, can be regarded as an assembly of N_A, A-type, and N_B, B-type, bare ions with charges Z_v^A and Z_v^B respectively, interacting with $N_e = N_A Z_v^A + N_B Z_v^B$ valence electrons through electron–ion potentials $v_A(r)$ and $v_B(r)$. Therefore, the total potential energy of the system can be written, within the Born–Oppenheimer approximation, as the sum of the direct ion–ion Coulombic interaction energy, and the ground state energy of the electronic system in the external potential created by the ions, $V_{ext}(\vec{r}, \{\vec{R}_l\}) = \sum_{i=A,B} \sum_{l(i)} v_i(|\vec{r} - \vec{R}_l|)$,

$$E(\{\vec{R}_l\}) = \frac{1}{2} \sum_{i,j=A,B} \sum_{l(i)\neq m(j)} \frac{Z_i Z_j}{|\vec{R}_l - \vec{R}_m|} + E_g[\rho_g(\vec{r}), V_{ext}(\vec{r}, \{\vec{R}_l\})], \tag{1}$$

Table 1. Input data for the Li–Mg alloys studied in this work, along with some simulation details. ρ is the total ionic number density taken from [20, 34].

$x = x_{\mathrm{Mg}}$	ρ (Å^{-3})	T (K)	N	Cutoff (Ryd)
0.30	0.040 71	887	800	18.25
0.50	0.040 41	887	800	18.15
0.70	0.040 11	887	800	18.00

where $\vec{R}_l$ are the ionic positions, the sum over $l(i)$ extends over the sites occupied by the i-type ions and $\rho_{\mathrm{g}}(\vec{r})$ is the ground state electronic density which, according to DFT, is obtained by minimizing the energy functional

$$E[\rho(\vec{r})] = T_{\mathrm{s}}[\rho] + E_{\mathrm{ext}}[\rho] + E_{\mathrm{H}}[\rho] + E_{\mathrm{xc}}[\rho], \tag{2}$$

where the terms represent, respectively, the electronic kinetic energy, $T_{\mathrm{s}}[\rho]$, of a non-interacting system with density $\rho(\vec{r})$, the energy of interaction with the external potential due to the ions, $E_{\mathrm{ext}}[\rho]$, the classical electrostatic energy (Hartree term), $E_{\mathrm{H}}[\rho]$, and the exchange–correlation energy, $E_{\mathrm{xc}}[\rho]$, for which we will adopt the local density approximation.

Within the KS-AIMD approach [2–4], $T_{\mathrm{s}}[\rho]$ is calculated exactly by using single-particle orbitals, which requires a huge computational effort. This is alleviated in the OF-AIMD approach [1, 22] by use of an explicit but approximate density functional for $T_{\mathrm{s}}[\rho]$. Proposed functionals consist of the von Weizsäcker term, $T_{\mathrm{W}}[\rho(\vec{r})] = \frac{1}{8}\int \mathrm{d}\vec{r}\,|\nabla\rho(\vec{r})|^2/\rho(\vec{r})$, plus other terms chosen to reproduce correctly some exactly known limits.

Here, we have used an averaged density model [23], where $T_{\mathrm{s}} = T_{\mathrm{W}} + T_\beta$,

$$T_\beta = \tfrac{3}{10}\int \mathrm{d}\vec{r}\,\rho(\vec{r})^{5/3-2\beta}\tilde{k}(\vec{r})^2 \tag{3}$$

$$\tilde{k}(\vec{r}) = (2k_{\mathrm{F}}^0)^3 \int \mathrm{d}\vec{s}\,k(\vec{s})w_\beta(2k_{\mathrm{F}}^0|\vec{r}-\vec{s}|) \tag{4}$$

where $k(\vec{r}) = (3\pi^2)^{1/3}\rho(\vec{r})^\beta$, k_{F}^0 is the Fermi wavevector corresponding to a mean electron density ρ_0 and $w_\beta(x)$ is a weight function determined by requiring the correct recovery of both the linear response theory and Thomas–Fermi limits. For reasons stated elsewhere, we have used a value of $\beta = 0.51$.

The other key ingredient is the local ionic pseudopotential, $v_{\mathrm{ps}}^\alpha(\vec{r})$, describing the ion–electron interaction. Its construction is fully described in [24] and we just mention that it has been constructed from first principles by fitting to a model of an ion immersed in a metallic medium.

In our simulations we consider N ions in a cubic cell with periodic boundary conditions. Given the ionic positions at time t, the electronic energy functional is minimized with respect to $\rho(\vec{r})$ represented by a single *effective orbital*, $\psi(\vec{r})$, defined as $\rho(\vec{r}) = \psi(\vec{r})^2$. The orbital is expanded in plane waves truncated at a cutoff energy, E_{Cut} (tables 1 and 5 specify both N and E_{Cut} for the systems and concentrations considered). The energy minimization with respect to the Fourier coefficients of the expansion is performed every time step using a quenching method which results in the ground state electronic density and energy. The forces on the ions are obtained from the electronic ground state via the Hellmann–Feynman theorem, and the ionic positions and velocities are updated by solving Newton's equations, with the Verlet leapfrog algorithm with a time step of 2.5×10^{-3} ps. In the simulations for the $\mathrm{Li}_x\mathrm{Mg}_{1-x}$ alloys, the equilibration lasted 5 ps and the calculation of properties was made averaging over 50 ps, whereas for the $\mathrm{Li}_x\mathrm{Ba}_{1-x}$ alloys the averaging was done over 90 ps.

3. Results: the Li–Mg system

The Li–Mg phase diagram shows that Li and Mg are completely miscible in the liquid state and even show some mild tendency towards heterocoordination. Ruppersberg *et al* [20] performed a neutron diffraction study of the total static structure factor, $S_T(q)$, for the 'zero-alloy' composition, namely $Li_{0.7}Mg_{0.3}$, at two temperatures $T = 695$ and 875 K. Their experimental results for both temperatures showed a rather structureless $S_T(q)$, suggesting some weak heterocoordination tendencies.

Until now, few theoretical works have studied the $Li_{1-x}Mg_x$ alloy system, and most of them have focused on the solid phase. Among those we mention [25] which calculates, for several concentrations, the elastic constants and the heat of mixing for the body centred cubic solid phase, using interatomic pair potentials derived from the Dagens *et al* [26] pseudopotentials. Hafner and co-workers [27, 28] have studied both the solid and liquid phases by using effective interatomic pair potentials derived from first-principles optimized pseudopotentials (OPW) of Harrison [29]. Although their results for the solid phase provided reasonable estimates of the enthalpies, volumes of formation, structure and stability range of the alloy phases, they failed to reproduce the experimental heterocoordination tendencies in the liquid phase. Within the framework of interatomic pair potentials derived from the neutral pseudoatom model, Canales *et al* have also studied the liquid alloy by means of both classical molecular dynamics (CMD) and liquid state theories [30] and obtained static structural results which satisfactorily accounted for the experimental ordering tendencies in the alloy. The same potentials were later used within CMD to study the dynamic properties of this alloy [31, 32], and interpreted recently in terms of the viscoelastic model for mixtures [33].

This work uses the OF-AIMD method to study the static and dynamic properties of the liquid $Li_{1-x}Mg_x$ alloy at $T = 887$ K and concentrations $x_{Mg} = 0.3$, 0.5 and 0.7. The experimental total ionic number densities were taken from [20, 34] and table 1 lists the specific thermodynamic states considered in this study.

First, we mention that OF-AIMD calculations on pure liquid Li and Mg at thermodynamic conditions near their respective triple points [35] yielded an accurate description for several static and dynamic properties. Figure 1 shows a comparison of the OF-AIMD static structure factors obtained with their experimental [36] counterparts; aside from overestimating somewhat the height of the main peak in Mg, we obtain a satisfactory agreement for the amplitude and phase of the oscillations as well as for their low q behaviour. As for the dynamical magnitudes, these are reported in the following subsections although we anticipate that the OF-AIMD results obtained will show a reasonable agreement with the experimental data. In this respect, the good results for the pure metals provide further confidence in the utility of the OF-AIMD method and the local ionic pseudopotentials when applied to the study of their binary alloys.

3.1. Structural properties

The simulations allow a direct evaluation of the partial pair distribution functions, $g_{ij}(r)$ as well as the corresponding partial Ashcroft–Langreth (AL) structure factors $S_{ij}(q)$, from which the total neutron weighted static structure factor, $S_T(q)$, is obtained as

$$S_T(q) = \frac{b_1^2 x_1 S_{11}(q) + b_2^2 x_2 S_{22}(q) + 2b_1 b_2 (x_1 x_2)^{1/2} S_{12}(q)}{x_1 b_1^2 + x_2 b_2^2} \tag{5}$$

where x_j and b_j ($j = 1, 2$) denote the concentration and neutron scattering length of the j-type component. To analyse possible ordering tendencies in a liquid binary alloy, the

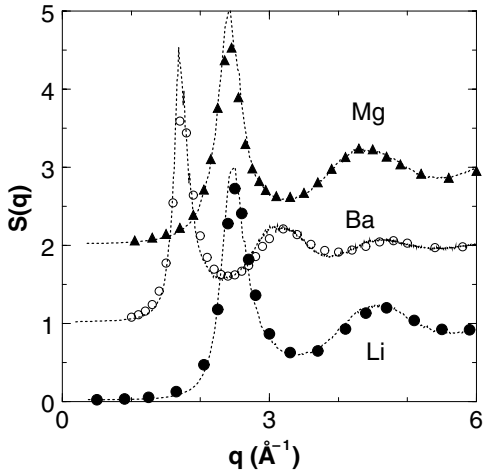

Figure 1. Static structure factors of liquid Li, Ba and Mg at their respective triple points. Dotted curves are the OF-AIMD results whereas the symbols are the experimental x-ray data of Waseda *et al* [36]. The $S(q)$ for Ba and Mg are displaced by one and two units respectively.

Bhatia–Thornton (BT) concentration–concentration, $S_{CC}(q)$, number–number, $S_{NN}(q)$, and number–concentration, $S_{NC}(q)$, partial structure factors [37] are ideally suited:

$$\begin{aligned} S_{CC}(q) &= x_1x_2[x_2S_{11}(q) + x_1S_{22}(q) - 2(x_1x_2)^{1/2}S_{12}(q)] \\ S_{NN}(q) &= x_1S_{11}(q) + x_2S_{22}(q) + 2(x_1x_2)^{1/2}S_{12}(q) \\ S_{NC}(q) &= S_{11}(q) - S_{22}(q) + (x_2 - x_1)/(x_1x_2)^{1/2}S_{12}(q). \end{aligned} \tag{6}$$

Moreover, in the case of the so-called 'zero-alloy' composition, i.e. when $x_1b_1 + x_2b_2 = 0$, then $S_{CC}(q) = x_1x_2S_{\mathrm{T}}(q)$ and, therefore, it can be directly probed by a single-neutron-scattering experiment. Figure 2 shows the OF-AIMD results for $S_{\mathrm{T}}(q)$ and $S_{CC}(q)$ along with the available experimental data for the 'zero-alloy' composition $Li_{0.7}Mg_{0.3}$. We observe that at this composition, the $S_{\mathrm{T}}(q)$ obtained accounts well for the main experimental features, with a value at $q \to 0$ which points to the existence of weak heterocoordination tendencies in the alloy. No experimental data are available for either $x_{\mathrm{Mg}} = 0.50$ and 0.70, but the present OF-AIMD results for their $S_{CC}(q)$ suggest a nearly ideal behaviour.

A simple way of analysing the short range order in the alloy is by means of the Warren–Cowley [38] short range order (SRO) parameter for the first-neighbour shell, $\alpha_1^{(i)}$, defined as

$$\alpha_1^{(i)} = 1 - \frac{n_{ij}}{x_j(n_{ii} + n_{ij})} \qquad (j \neq i = 1, 2), \tag{7}$$

where x_j is the concentration of the j-type particles and n_{ij} is the number of j-type particles around an i-type particle, within a spherical volume of radius R_{ij}. The n_{ij} can be calculated from the partial pair distribution functions, $g_{ij}(r)$, as follows:

$$n_{ij} = 4\pi\rho x_j \int_0^{R_{ij}} r^2 g_{ij}(r)\,\mathrm{d}r, \tag{8}$$

where R_{ij} is usually identified [39] with the position of the first minimum of the corresponding $g_{ij}(r)$. However, in those cases with a large size mismatch between the two components, it has been suggested that one take all R_{ij} as the position of the first minimum in the $g_{ii}(r)$ of the

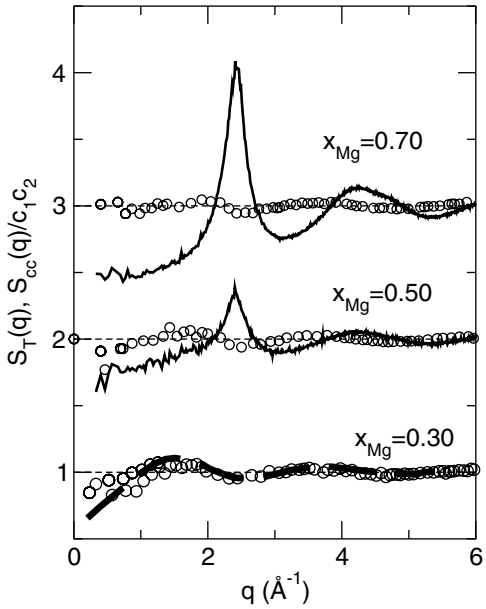

Figure 2. Concentration–concentration, $S_{CC}(q)$, and total static structure factors, $S_{\mathrm{T}}(q)$, for the liquid Li–Mg alloy at $T = 887$ K and three concentrations. Continuous curves and open circles are the OF-AIMD results for $S_{\mathrm{T}}(q)$ and $S_{CC}(q)$ respectively, whereas the broken line stands for the experimental neutron diffraction data of Ruppersberg *et al* [20] for $x_{\mathrm{Mg}} = 0.30$.

Table 2. Calculated values of the coordination numbers, n_{ij}, and the Warren–Cowley SRO parameters, $\alpha_1^{(i)}$, for the Li–Mg liquid alloy at $T = 887$ K.

x_{Mg}	n_{LiLi}	n_{LiMg}	n_{MgLi}	n_{MgMg}	$\alpha_1^{(\mathrm{Li})}$	$\alpha_1^{(\mathrm{Mg})}$
0.30	8.9	4.5	10.4	5.2	−0.12	0.05
0.50	6.2	7.5	7.5	8.6	−0.09	0.06
0.70	3.5	9.5	4.1	11.0	−0.04	0.10

larger component. For a random distribution of atoms $\alpha_1^{(i)} = 0$, whereas a positive (negative) value for $\alpha_1^{(i)}$ suggests a homocoordination (heterocoordination) tendency. We have evaluated both $\alpha_1^{(\mathrm{Li})}$ and $\alpha_1^{(\mathrm{Mg})}$ for the liquid $\mathrm{Li}_{1-x}\mathrm{Mg}_x$ alloy at $T = 887$ K and the results are shown in table 2. We obtain rather small values with opposite signs for $\alpha_1^{(\mathrm{Li})}$ and $\alpha_1^{(\mathrm{Mg})}$ which suggest a nearly ideal behaviour for all concentrations. This is corroborated by resorting to the local mole fractions method [40], which has also been used to analyse the ordering tendencies in mixtures. For a binary system, the local mole fractions, x_{ii}, are defined as

$$x_{ii} = \frac{n_{ii}}{n_{ii} + n_{ij}} \qquad j \neq i = 1, 2. \tag{9}$$

For a homogeneous phase, when the two species are nearly equally distributed, $x_{\mathrm{s}} - 1 = x_{11} + x_{22} - 1$ is around zero; whereas for a demixed state, particles of the same species dominate the distribution and $x_{\mathrm{s}} - 1$ grows [40]. Our calculated values of $x_{\mathrm{s}} - 1$ are close to zero ($\approx 10^{-3}$) for the three concentrations.

3.2. Dynamic properties

3.2.1. Single-particle dynamics. We have evaluated the relative velocity correlation functions (VCFs), $Z_{ij}(t)$, defined [41] as the time correlation function of the relative velocity of the centre of mass of species i with respect to the centre of mass of species j:

$$Z_{ij}(t) = \tfrac{1}{3}x_i x_j N\langle[\vec{u}_i(t) - \vec{u}_j(t)] \cdot [\vec{u}_i(0) - \vec{u}_j(0)]\rangle, \tag{10}$$

where N is the total number of particles, $\vec{u}_i(t) = N_i^{-1}\sum_{l(i)=1}^{N_i}\vec{u}_{l(i)}(t)$, N_i is the number of i-type particles and $\vec{u}_{l(i)}(t)$ is the velocity of the i-type particle $l(i)$. The $Z_{ij}(t)$ is decomposed into self-contributions, $Z_{ij}^0(t)$, and distinct contributions, $Z_{ij}^d(t)$:

$$Z_{ij}(t) = (1 - \delta_{ij})Z_{ij}^0(t) + x_i x_j Z_{ij}^d(t), \tag{11}$$

where δ_{ij} is Kronecker's delta, $Z_{ij}^0(t) = x_j Z_i^s(t) + x_i Z_j^s(t)$ and $Z_i^s(t)$ is the velocity autocorrelation function of a tagged i-type particle in the fluid. The time integrals of $Z_{ij}(t)$, $Z_{ij}^0(t)$, $Z_{ij}^d(t)$ and $Z_i^s(t)$ give the associated diffusion coefficients (DC), namely D_{ij}, D_{ij}^0, D_{ij}^d and D_i^s respectively, where D_i^s is the usual self-diffusion coefficient. From the previous expressions, we may write (we consider binary mixtures)

$$D_{12} = D_{12}^0 + x_1 x_2 D_{12}^d \equiv D_{12}^0(1 + \gamma_{12}), \tag{12}$$

with $D_{12}^0 = x_2 D_1^s + x_1 D_2^s$ and γ_{12} measures the deviation from an ideal mixture (i.e. when all species are identical, $\gamma_{12} = 0$). The interdiffusion coefficient is given as

$$D_{\text{int}} = \theta D_{12} \equiv \theta(1 + \gamma_{12})D_{12}^0, \tag{13}$$

where $\theta = x_1 x_2 / S_{CC}(q \to 0)$. For a nearly ideal mixture, $\theta \approx 1$, $\gamma_{12} \approx 0$ and therefore $D_{\text{int}} \approx D_{12}^0$.

The results for the self-VCF and relative VCF for the $Li_{1-x}Mg_x$ liquid alloy are shown in figure 3. The self-VCF of the heavier particles, $Z_{\text{Mg}}^s(t)$, has the slower decay and smaller backscattering as a result of the velocity persistence of the heavy particles when they collide with the lighter ones. When the concentration of the heavy particles is increased, the backscattering effect is enhanced because of there being more collisions of both heavy and lighter particles with the heavy ones; therefore both self-diffusion coefficients are decreased. In fact, table 2 shows that although the total number of nearest neighbours of a Li (or Mg) ion changes slightly with concentration, the number of the heavier Mg ions increases noticeably.

As for $Z_{\text{LiMg}}(t)$, it stands between the two self-VCFs, which suggests a negligible effect of the distinct correlations (with particles of either the same or different species). Quantitative information on the weight of the distinct effects on D_{LiMg} is provided by γ_{LiMg}, with positive (negative) values of γ_{LiMg} indicating [41, 42] that particles of the same (different) species have a greater tendency to diffuse together that those of distinct (the same) species. The results obtained are close to zero, for all concentrations, which indicates a nearly ideal behaviour.

No experimental data are available for the diffusion coefficients for the liquid $Li_{1-x}Mg_x$ alloy. However, in order to provide some confidence in the previous results, we note that OF-AIMD calculations for both pure Li and Mg at thermodynamic conditions near their respective triple points gave $D_{\text{Li}}^0 = 0.63$ and $D_{\text{Mg}}^0 = 0.52$ whereas the experimental values are (in units of 10^{-4} cm^2 s^{-1}) $D_{\text{Li}}^{\text{exp}} = 0.64 \pm 0.02$ [43] and $D_{\text{Mg}}^{\text{exp}} = 0.56 \pm 0.02$ [44]. In table 3 we also include the results for $S_{CC}(q \to 0) \cdot D_{\text{int}}$, which are very similar to those predicted by Darken's semiempirical expression [45], i.e. $S_{CC}(q \to 0) \cdot D_{\text{int}} = x_1 x_2 D_{12}^0$; this is another indicator of the petty role played by the distinct interparticle velocity correlations which are neglected in Darken's relation.

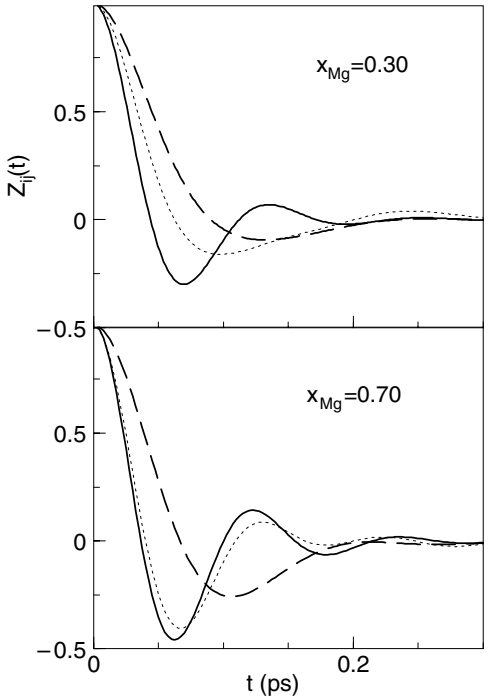

Figure 3. Normalized self-VACFs and relative VACFs for the liquid Li–Mg alloy at $T = 887$ K at two concentrations. The dotted, full and dashed curves represent $Z_{\mathrm{LiMg}}(t)$, $Z^{\mathrm{s}}_{\mathrm{Li}}(t)$ and $Z^{\mathrm{s}}_{\mathrm{Mg}}(t)$ respectively.

Table 3. Diffusion coefficients (in 10^{-4} cm^2 s^{-1}), for the Li–Mg liquid alloy at $T = 887$ K.

x_{Mg}	0.30	0.50	0.70
$D^{\mathrm{s}}_{\mathrm{Li}}$	1.63	1.17	0.73
$D^{\mathrm{s}}_{\mathrm{Mg}}$	1.17	0.87	0.55
D_{LiMg}	1.20	0.96	0.70
D^{0}_{LiMg}	1.30	1.02	0.68
D^{d}_{LiMg}	−0.48	−0.24	0.09
γ_{LiMg}	−0.08	−0.06	0.03
$S_{CC}(0)D_{\mathrm{int}}$	0.26	0.22	0.16
$S_{CC}(0)D^{(\mathrm{Darken})}_{\mathrm{int}}$	0.28	0.27	0.16

3.2.2. Collective dynamics. The density fluctuations in the alloy are usually described through the partial AL intermediate scattering functions, $F_{ij}(\vec{q}, t) = \langle \rho_i(\vec{q}, t) \cdot \rho^*_j(\vec{q}, 0)\rangle$, where

$$\rho_i(\vec{q}, t) = \frac{1}{\sqrt{N_i}} \sum_{l(i)=1}^{N_i} \exp[\mathrm{i}\vec{q} \cdot \vec{R}_{l(i)}(t)], \tag{14}$$

is the Fourier transform (FT) of the i-type component partial number density, N_i is the number of i-type particles, $\vec{R}_{l(i)}(t)$ is the position of the i-type particle l and $\langle \cdots \rangle$ stands for the ensemble average. The time Fourier transformation of the $F_{ij}(\vec{q}, t)$ into the frequency domain gives the partial dynamic structure factors $S_{ij}(\vec{q}, \omega)$ which are directly connected with the inelastic neutron scattering data.

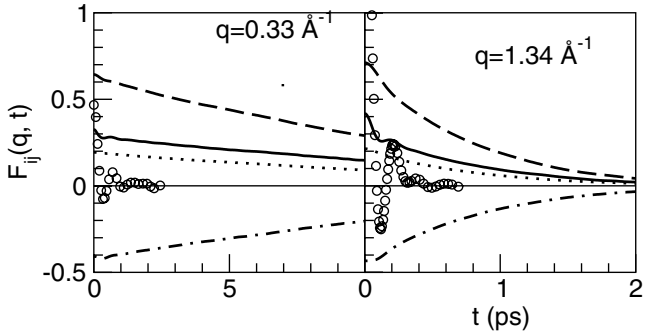

Figure 4. Partial intermediate scattering functions, $F_{ij}(q, t)$, at $q = 0.33$ and 1.34 Å^{-1}, for the liquid $Li_{0.7}Mg_{0.3}$ alloy at $T = 887$ K. The full, dashed, dot–dashed, open circles and dotted lines represent the $F_{\mathrm{LiLi}}(q, t)$, $F_{\mathrm{MgMg}}(q, t)$, $F_{\mathrm{LiMg}}(q, t)$, $10 \times F_{NN}(q, t)$ and $10 \times F_{CC}(q, t)$ respectively.

Another dynamical magnitude is the *i*-type component particle current

$$\vec{j}_i(\vec{q}, t) = \frac{1}{\sqrt{N_i}} \sum_{l=1}^{N_i} \vec{u}_{l(i)}(t) \exp[\mathrm{i}\vec{q} \cdot \vec{R}_{l(i)}(t)], \tag{15}$$

which is usually split into a longitudinal component, $j_i^{\mathrm{L}}(\vec{q}, t)$, parallel to $\vec{q}$, and a transverse component, $j_i^{\mathrm{T}}(\vec{q}, t)$, perpendicular to $\vec{q}$. Therefrom, the partial longitudinal, $C_{ij}^{\mathrm{L}}(\vec{q}, t)$, and transverse, $C_{ij}^{\mathrm{T}}(\vec{q}, t)$, current correlation functions are defined:

$$\begin{aligned} C_{ij}^{\mathrm{L}}(\vec{q}, t) &= \langle j_i^{\mathrm{L}}(\vec{q}, t) \cdot j_j^{\mathrm{L}*}(\vec{q}, 0) \rangle \\ C_{ij}^{\mathrm{T}}(\vec{q}, t) &= (1/2) \langle j_i^{\mathrm{T}}(\vec{q}, t) \cdot j_j^{\mathrm{T}*}(\vec{q}, 0) \rangle \end{aligned} \tag{16}$$

and their time FTs give the respective spectra, $C_{ij}^{\mathrm{L}}(\vec{q}, \omega)$ and $C_{ij}^{\mathrm{T}}(\vec{q}, \omega)$. We consider isotropic systems, and all the previous correlation functions depend on $q = \mid \vec{q} \mid$ only.

At low q values, the partial AL intermediate scattering functions, $F_{\mathrm{LiLi}}(q, t)$, $F_{\mathrm{MgMg}}(q, t)$ and $F_{\mathrm{LiMg}}(q, t)$ are dominated by the diffusive contributions which impose a very low decay; this is shown in figure 4 for $x_{\mathrm{Mg}} = 0.30$ but the same applies for the other concentrations. Those contributions mask the oscillations associated with the propagating density fluctuations, which however are exposed in the $F_{NN}(q, t)$. These results validate those obtained with effective pair potentials within CMD and the viscoelastic model [31, 33] which showed a similar behaviour. The density fluctuations appear as side peaks in the corresponding partial dynamic structure factors, $S_{ij}(q, \omega)$, which are shown in figure 5 for $q \approx 0.33$ Å^{-1}. At the three concentrations, $S_{\mathrm{LiLi}}(q, \omega)$, $S_{\mathrm{MgMg}}(q, \omega)$ and $S_{NN}(q, \omega)$ exhibit clear side peaks (or shoulders in the case of the MgMg partial for $x_{\mathrm{Mg}} = 0.30$), which at small q values are located at very similar frequencies; this is the usual behaviour in the hydrodynamic regime, and represents a propagating sound mode. $S_{NN}(q, \omega)$ reflects the average behaviour of the system and for $q \leqslant q_{\mathrm{h}}$ (where q_{h} denotes the upper limit of the hydrodynamic region), it exhibits a clear Rayleigh–Brillouin structure [46]. From the position, ω_{B}, of its Brillouin peak at the smallest q value reached by the simulations, namely $q \equiv q_{\mathrm{min}} \approx 0.23$ Å^{-1}, we can estimate the adiabatic velocity of propagation, $c_{\mathrm{s}} = \omega_{\mathrm{B}}/q$, of the sound modes in the alloy, i.e. $c_{\mathrm{s}} = 2400$ m s^{-1} (for $x_{\mathrm{Mg}} = 0.30$), $c_{\mathrm{s}} = 4000$ m s^{-1} ($x_{\mathrm{Mg}} = 0.50$) and $c_{\mathrm{s}} = 4550$ m s^{-1} ($x_{\mathrm{Mg}} = 0.70$). We are not aware of any measurement of c_{s} for this alloy; however, we mention that OF-AIMD calculations for both pure Li and Mg near their triple point gave $c_{\mathrm{s}} = 5000 \pm 150$ m s^{-1} and $c_{\mathrm{s}} = 4200 \pm 150$ m s^{-1} respectively, whereas the experimental values [44, 47] are ≈4550 and 4100 m s^{-1}.

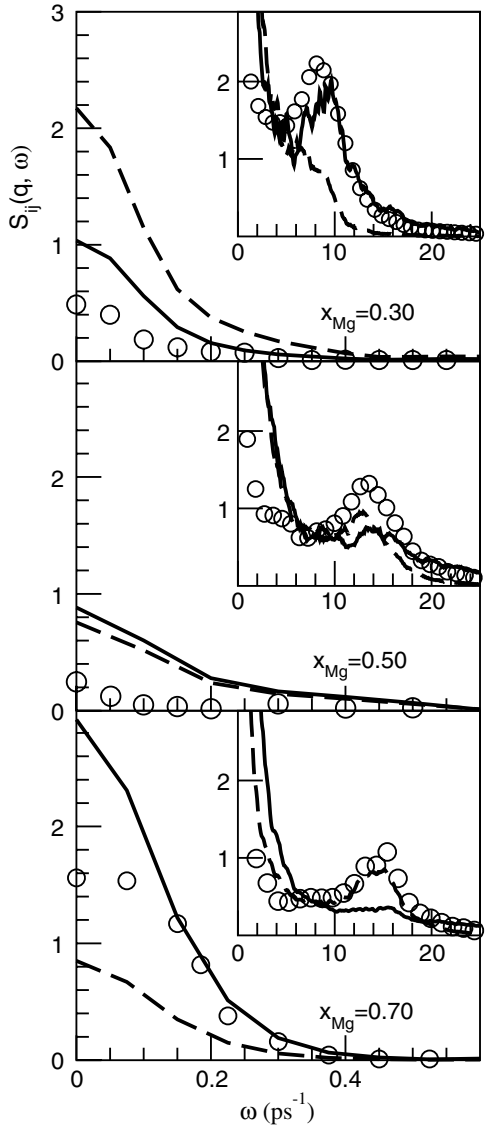

Figure 5. Partial dynamic structure factors, $S_{ij}(q,\omega)$, at $q = 0.33$ Å^{-1}, for the liquid Li–Mg alloy at $T = 887$ K and three concentrations. The full, dashed and circles curves represent the $S_{\mathrm{LiLi}}(q,\omega)$, $S_{\mathrm{MgMg}}(q,\omega)$ and $50 \times S_{NN}(q,\omega)$ respectively. The inset shows $10^3 S_{ij}(q,\omega)$.

In the case of the CMD simulations of the system with effective pair potentials [31, 33], the dominance of the diffusive component in the partial AL dynamic structure factors was extreme, and completely covered the propagating contribution, leading to peakless $S_{ij}(q,\omega)$ for small wavevectors. In these OF-AIMD simulations small side peaks are indeed obtained, whose range of existence depends on the concentration. For $\mathrm{Li}_{0.3}\mathrm{Mg}_{0.7}$, $S_{\mathrm{LiLi}}(q,\omega)$ and $S_{NN}(q,\omega)$ have peaks up to $q \approx 1.20$ Å^{-1} whereas those of $S_{\mathrm{MgMg}}(q,\omega)$ last until $q \approx 0.85$ Å^{-1}. On the other hand, for the $\mathrm{Li}_{0.7}\mathrm{Mg}_{0.3}$ alloy, $S_{\mathrm{MgMg}}(q,\omega)$ shows a side peak only at q_{min}, $S_{NN}(q,\omega)$ exhibits side peaks up to $q \approx 0.5$ Å^{-1}, whereas in $S_{\mathrm{LiLi}}(q,\omega)$ they appear up to $q \approx 1.4$ Å^{-1}.

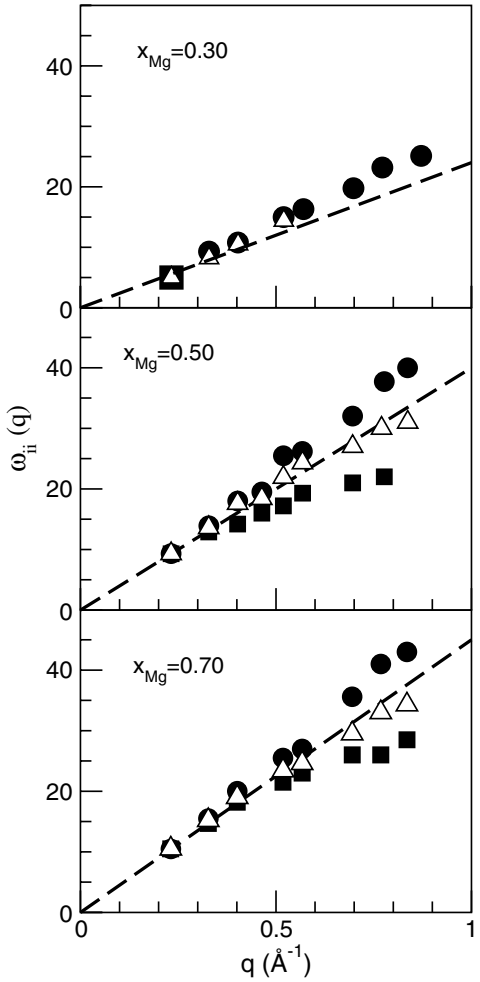

Figure 6. The dispersion relation of the collective modes in the partials, $S_{\mathrm{LiLi}}(q,\omega)$, $S_{\mathrm{MgMg}}(q,\omega)$ and $S_{NN}(q,\omega)$ (full circles, full squares and open triangles respectively), for the liquid Li–Mg alloy at $T = 887$ K and several concentrations. The slope of the dashed lines is the calculated adiabatic sound velocity.

From the positions of the side peaks, we obtain the associated dispersion curves, $\omega_{\mathrm{LiLi}}(q)$, $\omega_{\mathrm{MgMg}}(q)$ and $\omega_{NN}(q)$, which are depicted in figure 6. At q_{min}, the $\omega_{\mathrm{LiLi}}(q)$, $\omega_{\mathrm{MgMg}}(q)$ and $\omega_{NN}(q)$ virtually coincide, which means that for $q \leqslant q_{\mathrm{min}}$ the Li and Mg particles oscillate at the same frequency. However, for greater qs we observe that for $x_{\mathrm{Mg}} = 0.50$ and 0.70, the dispersion curve splits into two branches exposing two non-hydrodynamic (kinetic) modes, known as fast and slow sound modes, which signal the onset of a dynamic decoupling between the Li and Mg particles. The fast mode, which involves Li particles only, has a phase velocity, $c_{\mathrm{fast}} \approx 4600 \pm 200\,\mathrm{m\ s^{-1}}$, which is roughly the same at the two concentrations; in fact this result agrees with the predictions of the RET [8, 9], which states that the phase velocity of the fast mode should be very close to the adiabatic sound velocity of the corresponding light particle fluid, namely a pure Li system obtained by removing all the Mg particles. The previous results clearly show that when q diminishes towards q_{h}, the fast sound mode undergoes a continuous

transition into the hydrodynamic sound mode and the merging occurs at $0.2 \leqslant q \leqslant 0.3$ Å^{-1}. Moreover, the RET predicts that when the concentration of the light component is increased the fast mode will fade away, being overcome by the (extended) sound mode; this is precisely what we observe at $x_{\mathrm{Mg}} = 0.30$, where the dispersion curve $\omega_{\mathrm{LiLi}}(q)$ is rather close to the (extended) hydrodynamic sound mode.

Neither side peaks nor shoulders are observed in $S_{CC}(q,\omega)$ at any q value. This is explained by the dominance of the diffusive contributions in the $F_{ij}(q,t)$; however, the concentration modes may be exposed by the associated partial longitudinal current correlation function $C^{\mathrm{L}}_{CC}(q,\omega)$. In general, further information about longitudinal collective modes is provided by the partial longitudinal current correlation functions, $C^{\mathrm{L}}_{ij}(q,\omega) \equiv \omega^2 S^{\mathrm{L}}_{ij}(q,\omega)$, which have been evaluated according to equation (16), and are plotted in figures 7 and 8 for two q values.

For any q value, $C^{\mathrm{L}}_{\mathrm{LiLi}}(q,\omega)$, $C^{\mathrm{L}}_{\mathrm{MgMg}}(q,\omega)$, $C^{\mathrm{L}}_{NN}(q,\omega)$ and $C^{\mathrm{L}}_{CC}(q,\omega)$ exhibit at least one peak. In restricted q regions an additional second peak appears in all the partials except $C^{\mathrm{L}}_{\mathrm{MgMg}}(q,\omega)$, and in somewhat larger q regions the peaks become shoulders. For instance, at q_{min} (figure 7) we find for all concentrations two characteristic frequencies. At the low one, $C^{\mathrm{L}}_{\mathrm{LiLi}}(q,\omega)$, $C^{\mathrm{L}}_{\mathrm{MgMg}}(q,\omega)$ and $C^{\mathrm{L}}_{NN}(q,\omega)$ show a peak, and $C^{\mathrm{L}}_{CC}(q,\omega)$ a shoulder, located at the same position as the Brillouin peaks of the dynamic structure factors. Moreover, $C^{\mathrm{L}}_{\mathrm{LiMg}}(q,\omega)$ also displays a peak at the same frequency. This corroborates the quasi-hydrodynamic behaviour of the Mg particles and some of the Li ones for these small q values. At the high characteristic frequency, $C^{\mathrm{L}}_{\mathrm{LiLi}}(q,\omega)$ and $C^{\mathrm{L}}_{NN}(q,\omega)$ show a shoulder for $x_{\mathrm{Mg}} = 0.30$ and a peak for the other concentrations, whereas $C^{\mathrm{L}}_{CC}(q,\omega)$ displays a peak for all concentrations. Moreover $C^{\mathrm{L}}_{\mathrm{LiMg}}(q,\omega)$ has a minimum at this same frequency. This suggests that some Li particles are completely decoupled from the Mg ones, and move in opposite phase, indicating an optical character of this mode. At larger q values (figure 8) the system is of course not quasi-hydrodynamic any more, but still two characteristic frequencies appear. At the lower one a peak appears for the MgMg and NN partials, and at the higher frequency one finds a peak in the LiLi and CC partials, a shoulder in the NN partial and a minimum in the LiMg partial, indicating again the optical character of this high frequency mode.

From the positions of the previous peaks, the longitudinal dispersion relations, $\omega^{\mathrm{L}}_{\mathrm{LiLi}}(q)$, $\omega^{\mathrm{L}}_{\mathrm{MgMg}}(q)$, $\omega^{\mathrm{L}}_{NN}(q)$ and $\omega^{\mathrm{L}}_{CC}(q)$ are obtained (figure 9). The values of $\omega^{\mathrm{L}}_{\mathrm{MgMg}}(q)$ are always smaller than those of $\omega^{\mathrm{L}}_{\mathrm{LiLi}}(q)$, because of the greater atomic mass of Mg. For all concentrations, $\omega^{\mathrm{L}}_{\mathrm{MgMg}}(q)$ has one branch only, whereas $\omega^{\mathrm{L}}_{\mathrm{LiLi}}(q)$ and $\omega^{\mathrm{L}}_{NN}(q)$ exhibit for $x_{\mathrm{Mg}} = 0.50$ and 0.70 two branches, with the low frequency branch having a limited extent which includes the hydrodynamic region. This is because at these two concentrations, (figures 7 and 8) when q decreases (i.e. going into the hydrodynamic regime), the $C^{\mathrm{L}}_{\mathrm{LiLi}}(q,\omega)$ (and $C^{\mathrm{L}}_{NN}(q,\omega)$ too) develop two peaks, with the low frequency one situated close to that of $C^{\mathrm{L}}_{\mathrm{MgMg}}(q,\omega)$, and the high frequency peak being at frequencies similar to those of the pure Li system, although it vanishes as q diminishes towards the hydrodynamic region. This behaviour suggests that in the binary alloy the heavy Mg particles always keep their characteristic low frequencies whereas the lighter Li particles have a much higher frequency which is mostly kept when approaching the hydrodynamic regime, although as q decreases some Li particles start 'catching' the low frequency of the heavy Mg particles. Obviously, in the hydrodynamic ($q \to 0$) limit, all the particles must oscillate with the same frequency and therefore the $C^{\mathrm{L}}_{\mathrm{LiLi}}(q,\omega)$ (and $C^{\mathrm{L}}_{NN}(q,\omega)$) will only show the low frequency peak; the high frequency one vanishes.

As shown in figure 9, at low q values the $\omega^{\mathrm{L}}_{\mathrm{MgMg}}(q)$ has an initial linear increase up to a maximum followed by a minimum located at $q \approx 2.50$ Å^{-1} which coincides with the position of the main peak of $S_{\mathrm{MgMg}}(q)$. Similar behaviour is exhibited by the high frequency branch

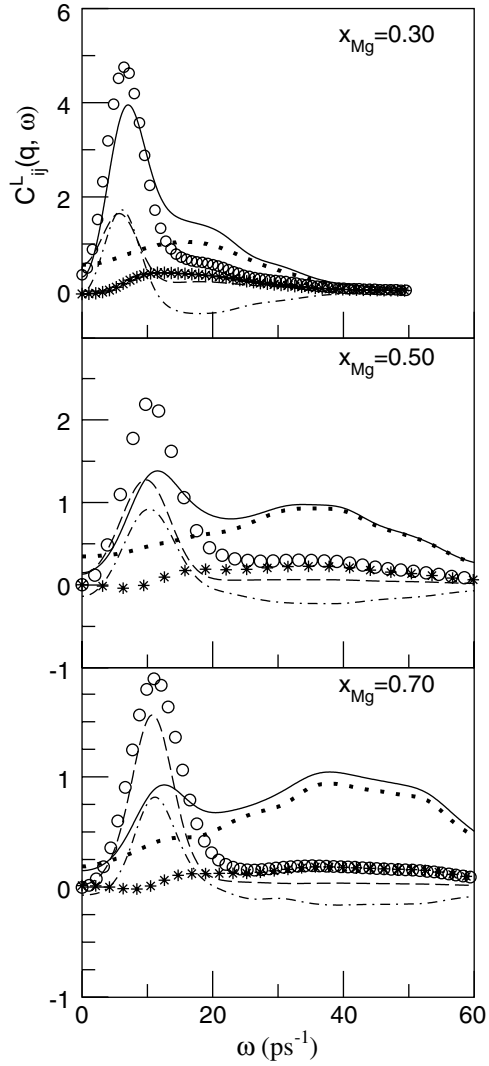

Figure 7. Partial longitudinal current correlation functions, $C^{\mathrm{L}}_{ij}(q,\omega)$, at $q = 0.23$ Å^{-1}, for the liquid Li–Mg alloy at $T = 887$ K and three concentrations. The full, dashed, dot–dashed, open circles, stars and dotted curves represent $C^{\mathrm{L}}_{\mathrm{LiLi}}(q,\omega)$, $C^{\mathrm{L}}_{\mathrm{MgMg}}(q,\omega)$, $C^{\mathrm{L}}_{\mathrm{LiMg}}(q,\omega)$, $C^{\mathrm{L}}_{NN}(q,\omega)$, $C^{\mathrm{L}}_{NC}(q,\omega)$ and $5 \times C^{\mathrm{L}}_{CC}(q,\omega)$ respectively.

of $\omega^{\mathrm{L}}_{\mathrm{LiLi}}(q)$, with a maximum and minimum at $\approx$1.5 Å^{-1} and 2.3 Å^{-1} respectively, which coincide with the first minimum and maximum of $S_{\mathrm{LiLi}}(q)$; moreover, as x_{Mg} is increased the structure of $\omega^{\mathrm{L}}_{\mathrm{LiLi}}(q)$ becomes less marked as a consequence of a similar trend in the maxima and minima of $S_{\mathrm{LiLi}}(q)$.

Depending on the concentration, the dispersion curves of both $\omega^{\mathrm{L}}_{NN}(q)$ and $\omega^{\mathrm{L}}_{CC}(q)$ have either one or two branches. As for the $\omega^{\mathrm{L}}_{NN}(q)$ curve, we note that it always has a branch associated with the majority component in the alloy and for $x_{\mathrm{Mg}} = 0.50$ and 0.70, a second branch appears. At both concentrations, the high frequency branch has a limited range and we observe that at small qs, the high frequency branch is induced by the Li particles only, whereas the low frequency branch comes from both the Li and Mg particles.

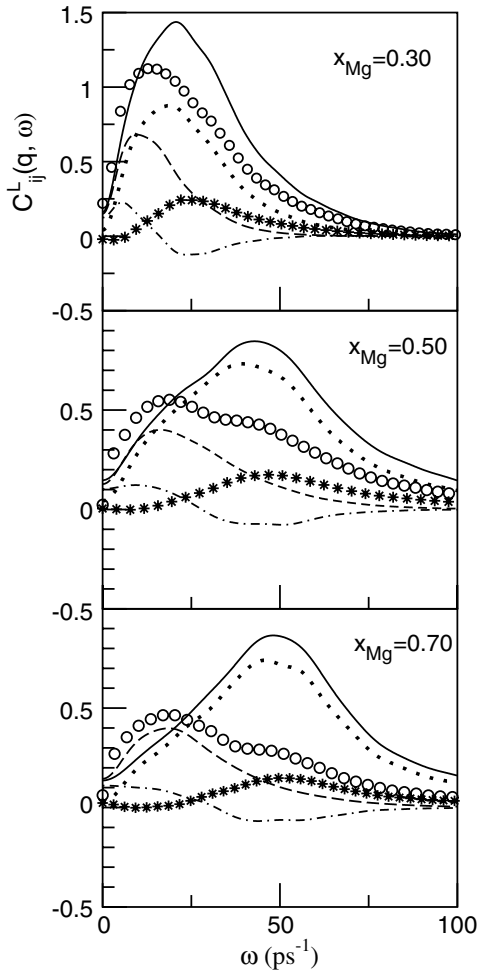

Figure 8. The same as the previous figure, but for $q = 2.4$ Å^{-1}.

Either one or two branches are exhibited by the $\omega^{\mathrm{L}}_{CC}(q)$ dispersion curve, as the $C^{\mathrm{L}}_{CC}(q, \omega)$, which is substantially smaller than the other partial currents, shows either one or two peaks which may be connected with propagating concentration modes. At low qs, including the hydrodynamic regime and for all concentrations, the $C^{\mathrm{L}}_{CC}(q, \omega)$ shows only one peak at a frequency higher than that of the $C^{\mathrm{L}}_{NN}(q, \omega)$ (figure 7). For qs well outside the hydrodynamic region, at $x_{\mathrm{Mg}} = 0.30$ and 0.50, two maxima are clearly visible in $C^{\mathrm{L}}_{CC}(q, \omega)$, one at a frequency close to the high frequency branch of $C^{\mathrm{L}}_{\mathrm{LiLi}}(q, \omega)$ and another at a frequency close to that of $C^{\mathrm{L}}_{\mathrm{MgMg}}(q, \omega)$, although this latter maximum becomes a shoulder at $x_{\mathrm{Mg}} = 0.70$.

Summing up, the high frequency branch of $\omega^{\mathrm{L}}_{CC}(q)$ exists for all concentrations, closely follows the high frequency $\omega^{\mathrm{L}}_{\mathrm{LiLi}}(q)$ and goes towards a finite value when $q \to 0$, which is a typical trend of the kinetic modes. On the other hand, the low frequency branch of $\omega^{\mathrm{L}}_{CC}(q)$ exists for $x_{\mathrm{Mg}} = 0.30$ and 0.50 only; it starts outside the hydrodynamic regime, closely follows $\omega^{\mathrm{L}}_{\mathrm{MgMg}}(q)$ and exists within a limited q range. In fact, we observe that as the x_{Mg} is increased, the gap between the $\omega^{\mathrm{L}}_{\mathrm{LiLi}}(q)$ and $\omega^{\mathrm{L}}_{\mathrm{MgMg}}(q)$ is somewhat decreased and this is the ultimate

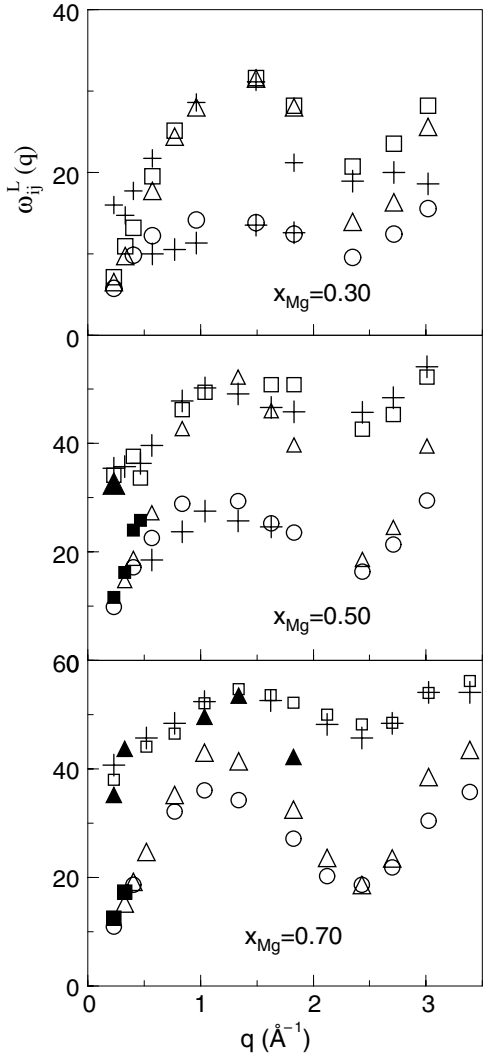

Figure 9. The longitudinal dispersion relation of the partials, $\omega^{\mathrm{L}}_{\mathrm{LiLi}}(q)$ (open and full squares), $\omega^{\mathrm{L}}_{\mathrm{MgMg}}(q)$ (open circles), number–number, $\omega^{\mathrm{L}}_{NN}(q)$ (open and full triangles) and concentration–concentration, $\omega^{\mathrm{L}}_{CC}(q)$ (plus signs) longitudinal modes, for the Li–Mg liquid alloy at $T = 887$ K and several concentrations.

reason for the disappearance of the low frequency branch of $\omega^{\mathrm{L}}_{CC}(q)$. Finally, it is worth stressing that, notwithstanding whether one or two $\omega^{\mathrm{L}}_{CC}(q)$ branches appear, there is always one branch associated with the minority component.

3.2.3. Transverse currents. The partial transverse current correlation functions, $C^{\mathrm{T}}_{ij}(q, \omega)$, inform us about the existence of shear modes in the system. These modes are not connected with any measurable magnitude and can only be analysed within a theoretical model or by resorting to MD simulations. Among the scant studies on transverse currents in liquids, most have addressed one-component systems where $C^{\mathrm{T}}(q, \omega)$ evolves from a Gaussian (when $q \to \infty$) towards a Lorentzian curve (when $q \to 0$). Both limiting cases preclude the possibility of

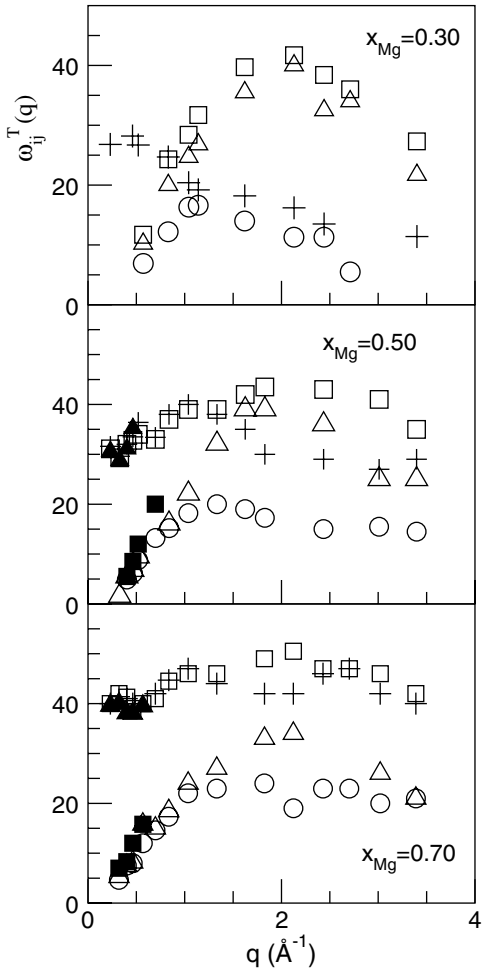

Figure 10. The transverse dispersion relation of the partials, $\omega^{\mathrm{T}}_{\mathrm{LiLi}}(q)$ (open and full squares), $\omega^{\mathrm{T}}_{\mathrm{MgMg}}(q)$ (open circles), number–number, $\omega^{\mathrm{T}}_{NN}(q)$ (open and full triangles) and concentration–concentration, $\omega^{\mathrm{T}}_{CC}(q)$ (plus signs) transverse modes, for the Li–Mg liquid alloy at $T = 887$ K and three concentrations.

propagation of the transverse modes, but at intermediate qs, the $C^{\mathrm{T}}(q, \omega)$ exhibits a peak which is connected with propagating shear waves.

The first CMD simulations of transverse current correlations in binary systems were performed on molten salts [48], where it was found that $C^{\mathrm{T}}_{NN}(q, \omega)$ behaves similarly to $C^{\mathrm{T}}(q, \omega)$, showing a peak at intermediate q values. Likewise, the charge–charge transverse current correlation functions showed a peak at both low and intermediate qs which was related to the existence of transverse optic modes which take a finite value in the hydrodynamic limit. Subsequent CMD studies in binary Lennard-Jones [10] systems have found optic-like modes associated with $C^{\mathrm{T}}_{CC}(q, \omega)$. Similar results have also been obtained in the CMD studies by Anento and Padró [32] for the liquid Li–Mg, Li–Na and Li_4Pb alloys.

We have calculated the partial transverse currents, $C^{\mathrm{T}}_{ij}(q, \omega)$, and from their respective peak positions, the corresponding transverse dispersion relations, $\omega^{\mathrm{T}}_{ij}(q)$, are obtained (figure 10).

$\omega^{\mathrm{T}}_{\mathrm{MgMg}}(q)$ has one branch whereas both $\omega^{\mathrm{T}}_{\mathrm{LiLi}}(q)$ and $\omega^{\mathrm{T}}_{NN}(q)$ evolve from one to two branches as x_{Mg} increases; this is the same trend as was already observed in the longitudinal dispersion relation. Moreover, the peak in $C^{\mathrm{T}}_{\mathrm{MgMg}}(q,\omega)$ and the low frequency peak in the $C^{\mathrm{T}}_{\mathrm{LiLi}}(q,\omega)$ coincide with a maximum in the $C^{\mathrm{T}}_{\mathrm{LiMg}}(q,\omega)$ which points to in-phase motion of some Li ions with the Mg ions.

The low frequency branch, $\omega^{\mathrm{T}}_{NN}(q)$, shows typical features of the one-component system, namely it starts at a q_{c}, exhibits a linear behaviour for low q values and goes to zero as $q \to q_{\mathrm{c}}$. The slope in the linear region assuming $\omega^{\mathrm{T}}_{NN}(q) \sim c_{\mathrm{T}}(q - q_{\mathrm{c}})$ yields an estimate of the velocity of propagation of the shear modes in the alloy: $c_{\mathrm{T}} \approx 2900$ and 2600 m s^{-1} for $x_{\mathrm{Mg}} = 0.30$ and 0.70 respectively. For the pure components we have obtained $c_{\mathrm{T}} \approx 3700$ m s^{-1} for pure Li at $T = 590$ K and $c_{\mathrm{T}} \approx 2600$ m s^{-1} for pure Mg at melting ($T = 953$ K). Also, in this linear region the low frequency branch $\omega^{\mathrm{T}}_{NN}(q)$ remains close to both $\omega^{\mathrm{T}}_{\mathrm{MgMg}}(q)$ and the low frequency branch $\omega^{\mathrm{T}}_{\mathrm{LiLi}}(q)$, which implies that the propagation of shear modes involves both species.

The CMD calculations of Anento and Padró [32] for the liquid Li–Mg alloy yielded transverse dispersion relations for $x_{\mathrm{Mg}} = 0.30$ which virtually coincided with the present results; however, they did not expose the high frequency $\omega^{\mathrm{T}}_{NN}(q)$ branches at $x_{\mathrm{Mg}} = 0.50, 0.70$ or the low frequency $\omega^{\mathrm{T}}_{\mathrm{LiLi}}(q)$ branch at $x_{\mathrm{Mg}} = 0.70$.

The small values taken by the $C^{\mathrm{T}}_{NC}(q,\omega)$ suggest weak couplings between density and concentration modes. The small magnitude of the $C^{\mathrm{T}}_{CC}(q,\omega)$, particularly at small qs, also underlines a weak contribution to the collective transverse dynamics. However, for the three concentrations we observe clear peaks in the $C^{\mathrm{T}}_{CC}(q,\omega)$ which already exist at q_{min}, leading to an $\omega^{\mathrm{T}}_{CC}(q)$ branch which takes a finite value as $q \to 0$. The peaks in $C^{\mathrm{T}}_{CC}(q,\omega)$ are a result of both the peak in the $C^{\mathrm{T}}_{\mathrm{LiLi}}(q,\omega)$ and a minimum in $C^{\mathrm{T}}_{\mathrm{LiMg}}(q,\omega)$ which is related to out-of-phase motion of particles of different species. Similar behaviour in molten salts has been associated with transverse optic modes of kinetic character [10, 48].

The alloy shear viscosity may be computed from the previous results by using the total transverse current correlation function $C^{\mathrm{T}}_{tt}(q,t) = \langle j^{\mathrm{T}}_t(q,t) j^{\mathrm{T}*}_t(q,0)\rangle$ where $j^{\mathrm{T}}_t(q,t) = x_1^{1/2} m_1 j^{\mathrm{T}}_1(q,t) + x_2^{1/2} m_2 j^{\mathrm{T}}_2(q,t)$ is the total transverse current, and the $j^{\mathrm{T}}_i(q,t)$ are defined according to equation (15). In the hydrodynamic limit [49], $C^{\mathrm{T}}_{tt}(q \to 0, t) = (\bar{m}/\beta)\exp\{-q^2\eta \mid t \mid /\bar{m}\rho\}$, where $\bar{m} = x_1 m_1 + x_2 m_2$ and η is the alloy shear viscosity. In terms of its memory function representation

$$\tilde{C}^{\mathrm{T}}_{tt}(q,z) = \frac{1}{\beta\bar{m}}\left[z + \frac{q^2}{\rho m}\tilde{\eta}(q,z)\right]^{-1}, \tag{17}$$

where the tilde denotes the Laplace transform, a generalized alloy shear viscosity coefficient, $\tilde{\eta}(q,z)$, is introduced. The area under the normalized $C^{\mathrm{T}}_{tt}(q,t)$ gives $\beta\bar{m}\tilde{C}^{\mathrm{T}}_{tt}(q, z=0)$, from which values for $\tilde{\eta}(q, z=0)$ are derived and, when extrapolated to $q = 0$, give the alloy shear viscosity η. The calculated values for η are shown in table 4, although no experimental data are as yet available for the alloy shear viscosities. However, we mention that the OF-AIMD calculations for both pure Li and Mg at thermodynamic conditions near their corresponding triple points gave $\eta_{\mathrm{Li}} = 0.61 \pm 0.05$ and $\eta_{\mathrm{Mg}} = 1.16 \pm 0.1$ whereas their respective experimental values are (in GPa ps) $\eta^{\mathrm{exp}}_{\mathrm{Li}} = 0.57 \pm 0.10$ [43] whereas $\eta^{\mathrm{exp}}_{\mathrm{Mg}} = 1.25 \pm 0.15$ [44]. For simple liquid alloys, η shows either a linear or a small negative deviation from the linear law, whereas positive deviations are usually exhibited by those alloys with heterocoordination tendencies. The calculated results show a virtually linear behaviour, which sounds plausible on account of the mild heterocoordination tendencies found for this alloy.

Table 4. Calculated values of the shear viscosity η (in GPa ps) for the Li–Mg liquid alloy at $T = 887$ K.

x_{Mg}	η_{Th}
0.30	0.50 ± 0.05
0.50	0.75 ± 0.05
0.70	1.07 ± 0.08

Table 5. Input data for the Li–Ba alloys studied in this work, along with some simulation details. ρ is the total ionic number density taken from [21, 51].

$x = x_{Ba}$	ρ (Å^{-3})	T (K)	N	Cutoff (Ryd)
0.12	0.036 3889	575	1200	12.75
0.30	0.027 877	575	600	17.50
0.59	0.020 518	775	600	14.25

4. Results: the Li–Ba system

Experimental work performed on the $Li_{1-x}Ba_x$ alloy is rather scarce. Even its phase diagram is not yet fully settled as two rather different phase diagrams have been proposed [50, 51]. Whereas one gives a eutectic composition at $x_{Ba} = 0.10$ and an intermetallic compound Li_4Ba, the other phase diagram locates the eutectic composition at $x_{Ba} = 0.20$ and reports two intermetallic compounds $LiBa_2$ and $LiBa_6$. Ruppersberg and co-workers [51] have measured the density, compressibility, heat capacity and surface tension of the liquid Li–Ba alloy at several concentrations and temperatures; moreover, NS experiments were performed [21] for $x_{Ba} = 0.12$, 0.30 and $T = 575$ K (the latter corresponding to the 'zero-alloy' composition) and $x_{Ba} = 0.59$ and $T = 775$ K. The total static structure factors, $S_T(q)$, showed a marked composition dependence and the data for $S_{CC}(q \to 0)$ suggested weak homocoordination (heterocoordination) tendencies for $x_{Ba} = 0.12$ and 0.30 ($x_{Ba} = 0.59$).

A similar scarcity of results is found on the theoretical side, as we are aware of just two calculations. First, we mention a structural study [21] performed using the hard sphere (HS) model within the Percus–Yevick analytical solution for HS binary mixtures. The results obtained for the $S_T(q)$ showed a qualitative agreement with experiment although the amplitude of the oscillations was grossly overestimated and significant discrepancies appear when $q \to 0$. Subsequently, a more elaborate approach was taken by González *et al* [52] who studied the static structure of liquid $Li_{0.88}Ba_{0.12}$ alloy by using effective interatomic pair potentials derived within the neutral pseudoatom model (NPA) [53] and the modified hypernetted chain (MHNC) theory [54] to obtain the liquid static structure. Their calculated $S_T(q)$ substantially improved on the previous HS-based calculations, but no further magnitudes were evaluated.

This work presents an AIMD study of the liquid $Li_{1-x}Ba_x$ alloy at the same thermodynamic states for which the NS experiments [21] were performed. Table 5 provides information about the thermodynamic states considered in this study along with other technical simulation details. First, we note that an OF-AIMD calculation for pure liquid Ba at thermodynamic conditions near its triple point provided a fair description of several static and dynamic properties, although the results were not so accurate as those already attained for liquid Li and Mg. Figure 1 shows the OF-AIMD static structure factor obtained for liquid Ba which qualitatively agrees with the experimental data [36], but overestimates the height of the main peak and shows some dephasing in the oscillations. Further results concerning some dynamical magnitudes are reported in the ensuing subsections.

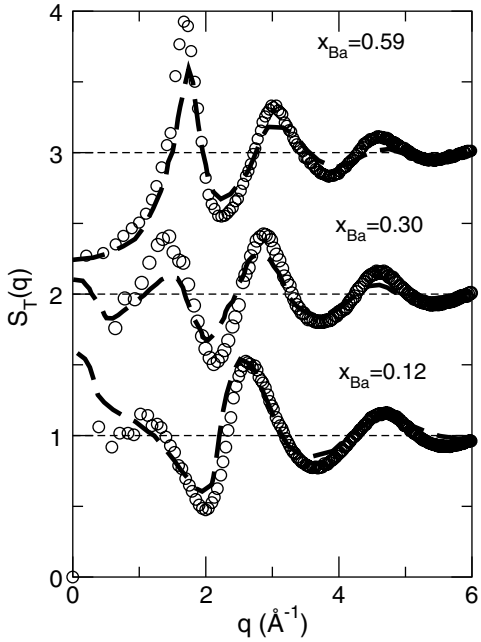

Figure 11. Total static structure factors, $S_{\mathrm{T}}(q)$, for the liquid Li–Ba alloy at $x_{\mathrm{Ba}} = 0.12$, 0.30 and $T = 575$ K and $x_{\mathrm{Ba}} = 0.59$ and $T = 775$ K. Open circles are the OF-AIMD results for $S_{\mathrm{T}}(q)$ whereas the broken line shows the experimental neutron diffraction data of Ruppersberg [21].

4.1. Structural properties

We have calculated the partial pair distribution functions, $g_{ij}(r)$ and the associated AL partial structure factors $S_{ij}(q)$, although comparison with the experimental data can only be performed at the level of the $S_{\mathrm{T}}(q)$. As shown in figure 11, the calculated OF-AIMD $S_{\mathrm{T}}(q)$ qualitatively reproduce the main features of the experiment [21], although there is some underestimation for the amplitude of the oscillations and when $q \to 0$ some discrepancies appear for $x_{\mathrm{Ba}} = 0.12$ and 0.30.

To analyse the short range order in the alloy, we have used the local mole fractions method [40] which was already described in the previous section. This is more appropriate for those systems with a large atomic size mismatch between the two components [11] and we have taken all the R_{ij} in equation (8) as the position of the first minimum of $g_{\mathrm{BaBa}}(r)$. Table 6 shows the calculated values for $x_{\mathrm{s}} - 1$ which, for $x_{\mathrm{Ba}} = 0.12$ and 0.30, are small and positive numbers indicating a mild homocoordination tendency, whereas a negative value is obtained at $x_{\mathrm{Ba}} = 0.59$ which now suggests a heterocoordination tendency. In all cases, the previous tendencies agree with the experimental data [21]. It is worth noting that the corresponding Warren–Cowley [38] SRO parameters also take positive values at $x_{\mathrm{Ba}} = 0.12$ and 0.30, which signals an homocoordination tendency, whereas for $x_{\mathrm{Ba}} = 0.59$ the two parameters take opposite signs leading to inconclusive results.

4.2. Dynamic properties

4.2.1. Single-particle dynamics. The results obtained for the self-VCFs and relative VCFs of the $\mathrm{Li}_{1-x}\mathrm{Ba}_x$ liquid alloy are shown in figure 12. Now the $Z^{\mathrm{s}}_{\mathrm{Ba}}(t)$ has the slower decay and

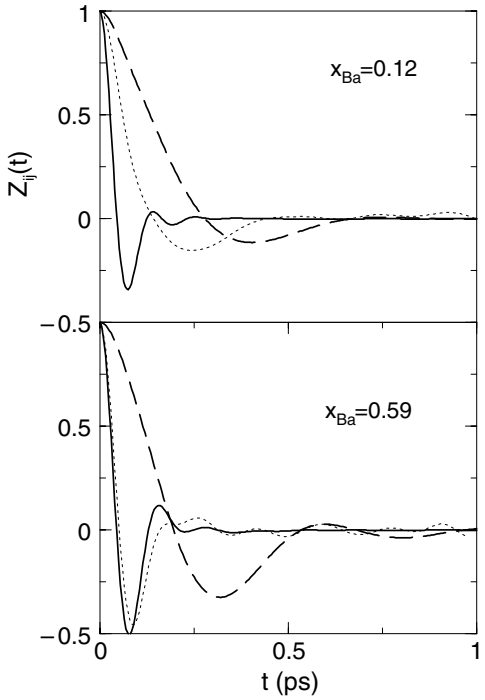

Figure 12. Normalized self-VACFs and relative VACFs for the liquid $Li_{0.88}Ba_{0.12}$ alloy at $T = 575$ and $Li_{0.41}Ba_{0.59}$ alloy at $T = 775$. The dotted, full and dashed curves represent $Z_{\mathrm{LiBa}}(t)$, $Z^{\mathrm{s}}_{\mathrm{Li}}(t)$ and $Z^{\mathrm{s}}_{\mathrm{Ba}}(t)$ respectively.

Table 6. Calculated values of the Warren–Cowley SRO parameters, $\alpha_1^{(i)}$, for the Li–Ba liquid alloy at the thermodynamic states considered in this work.

x_{Ba}	$\alpha_1^{(\mathrm{Li})}$	$\alpha_1^{(\mathrm{Ba})}$	$x_{\mathrm{s}} - 1$
0.12	0.05	0.0	0.003
0.30	0.014	0.0	0.005
0.59	−0.12	0.15	−0.01

smaller backscattering, although when the concentration of the heavy particles is increased, the backscattering effect increases and both self-diffusion coefficients decrease. The $Z_{\mathrm{LiBa}}(t)$ stands between the two self-VCFs, and the very small positive values of γ_{LiBa} at $x_{\mathrm{Ba}} = 0.12$ and 0.30 again lead to prediction of a rather mild homocoordination behaviour whereas the negative γ_{LiBa} at $x_{\mathrm{Ba}} = 0.59$ indicates heterocoordination tendencies.

No experimental data are available for the diffusion coefficients in the liquid $Li_{1-x}Ba_x$ alloy; even that of pure Ba has not yet been measured. The OF-AIMD calculations for pure liquid Ba near the triple point produced a value $D^0_{\mathrm{Ba}} = 0.19 \pm 0.02$ (in units of 10^{-4} cm^2 s^{-1}), which is comparable to other calculated values [55]. Table 3 includes also the results for $S_{CC}(q \to 0) \cdot D_{\mathrm{int}}$, which are similar to those obtained from Darken's semiempirical expression.

4.2.2. Collective dynamics. The calculated AL partial intermediate scattering functions, $F_{ij}(q, t)$, show a behaviour similar to that for the Li–Mg alloy, with the diffusive contributions playing a dominant role at low qs. Therefore, the investigation of possible propagating

Table 7. Diffusion coefficients (in 10^{-4} cm^2 s^{-1}) for the Li–Ba liquid alloy at $T = 575$ K ($x_{\rm Ba} = 0.12$, 0.30) and 775 K ($x_{\rm Ba} = 0.59$).

$x_{\rm Ba}$	0.12	0.30	0.59
$D^{\rm s}_{\rm Li}$	0.78	0.48	0.54
$D^{\rm s}_{\rm Ba}$	0.39	0.22	0.24
$D_{\rm LiBa}$	0.47	0.30	0.39
$D^{0}_{\rm LiBa}$	0.44	0.30	0.42
$D^{d}_{\rm LiBa}$	0.28	0	−0.12
$\gamma_{\rm LiBa}$	0.07	0	−0.30
$S_{CC}(0)D_{\rm int}$	0.054	0.062	0.111
$S_{CC}(0)D^{\rm (Darken)}_{\rm int}$	0.047	0.063	0.093

longitudinal modes is better performed in terms of the associated partial dynamic structure factors. Figure 13 shows the $S_{\rm LiLi}(q,\omega)$, $S_{\rm BaBa}(q,\omega)$ and $S_{NN}(q,\omega)$ calculated at the lowest wavevector allowed by the simulation, i.e. $q_{\rm min} = 0.19, 0.22$ and 0.20 Å^{-1} for $x_{\rm Ba} = 0.12, 0.30$ and 0.59 respectively. We stress that at these lowest wavevectors, the hydrodynamic region has not yet been reached. Whereas at $x_{\rm Ba} = 0.30$ and 0.59 the small difference between the peak positions of the corresponding $S_{ij}(q,\omega)$ suggest that $q_{\rm min}$ must be close to $q_{\rm h}$, for $x_{\rm Ba} = 0.12$ there is still an appreciable mismatch between the peak positions of $S_{\rm LiLi}(q,\omega)$ and $S_{\rm BaBa}(q,\omega)$ (located at $\approx$5.1 and 3.7 ps^{-1} respectively). Therefore, the previous results show that the transition towards the hydrodynamic regime takes place at smaller q values than in the Li–Mg alloy and consequently the hydrodynamic regime comprises a smaller range of wavevectors. From the position of the side peaks in $S_{NN}(q,\omega)$, we have estimated the adiabatic sound velocity in the alloy, i.e. $c_{\rm s} = 2500$ m s^{-1} (for $x_{\rm Ba} = 0.12$), $c_{\rm s} = 2000$ m s^{-1} ($x_{\rm Ba} = 0.30$) and $c_{\rm s} = 1700$ m s^{-1} ($x_{\rm Ba} = 0.59$) which compare well with the experimental [51] values of 2550, 1900 and 1500 m s^{-1} respectively.

The dispersion relations, as derived from the peak positions, are shown in figure 14. At the three concentrations, we observe a splitting into fast and slow kinetic modes. Note that the difference in slope between the two modes is substantially greater than that for the Li–Mg alloy, because of the greater mass difference (and, therefore, oscillation frequency difference) of the Li and Ba ions. Moreover, the hydrodynamic regime is now attained at a smaller q as it becomes harder for the lighter Li ions to oscillate with the same frequency as the much heavier Ba ions because of the increased difference between their natural oscillation frequencies. It is also observed that the fast sound mode still appears at the smallest concentration of the heavy Ba particles considered, namely $x_{\rm Ba} = 0.12$, which complies with the RET prediction that the increase of the mass ratio and/or the decrease of the number density widens the concentration range for the existence of both modes.

In order to uncover additional longitudinal modes, we have again computed the partial longitudinal current correlation functions, and the positions of their respective peaks give rise to the corresponding longitudinal dispersion relations which are plotted in figure 15. These dispersion relations show the same basic trends as were already found for the Li–Mg liquid alloy, namely: (i) the heavier component has one dispersion branch, $\omega^{\rm L}_{\rm BaBa}(q)$, which hardly changes with concentration; (ii) both the lighter component, $\omega^{\rm L}_{\rm LiLi}(q)$, and $\omega^{\rm L}_{NN}(q)$ evolve from one to two branches as the concentration of the heavier component increases; and (iii) the $\omega^{\rm L}_{CC}(q)$ always has a high frequency branch which takes a finite value when $q \to 0$, as well as a low frequency one which disappears when the concentration of the heavier component increases.

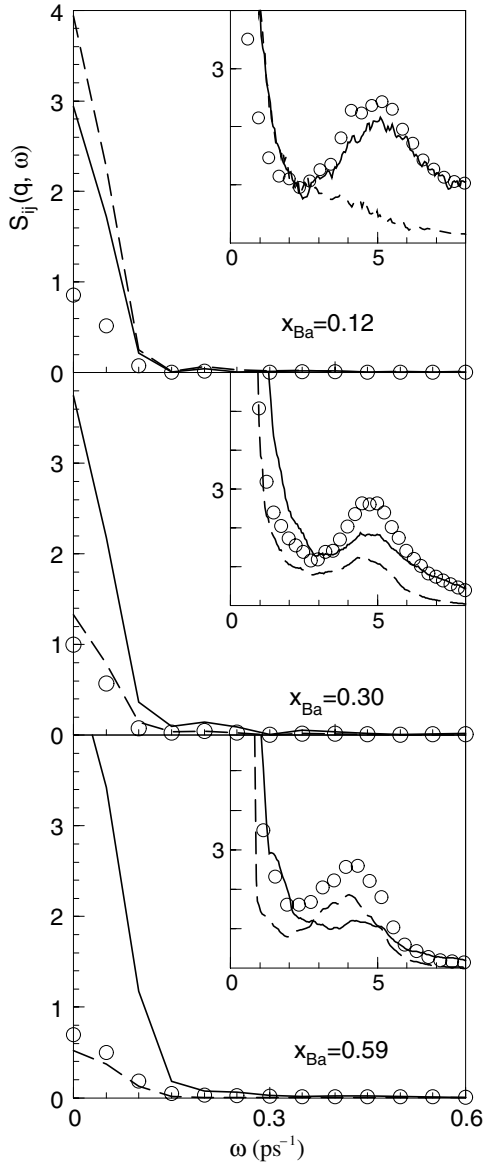

Figure 13. Partial dynamic structure factors, $S_{ij}(q,\omega)$, at $q = 0.19$ Å^{-1} ($x_{\mathrm{Ba}} = 0.12$, $T = 575$ K), $q = 0.23$ Å^{-1} ($x_{\mathrm{Ba}} = 0.30$, $T = 575$ K) and $q = 0.20$ Å^{-1} ($x_{\mathrm{Ba}} = 0.59$, $T = 775$ K), for the liquid Li–Ba alloy. The full, dashed and circles curves represent $S_{\mathrm{LiLi}}(q,\omega)$, $S_{\mathrm{BaBa}}(q,\omega)$ and $S_{NN}(q,\omega)$ respectively. The inset shows $10^3 S_{ij}(q,\omega)$.

The transverse currents, $C^{\mathrm{T}}_{ij}(q,\omega)$, have been calculated and the associated transverse dispersion relations, $\omega^{\mathrm{T}}_{ij}(q)$, are plotted in figure 16. $\omega^{\mathrm{T}}_{\mathrm{BaBa}}(q)$ always has one branch whereas both $\omega^{\mathrm{T}}_{\mathrm{LiLi}}(q)$ and $\omega^{\mathrm{T}}_{NN}(q)$ develop a second branch as the concentration of the heavier component increases. However, at $x_{\mathrm{Ba}} = 0.12$, $\omega^{\mathrm{T}}_{\mathrm{LiLi}}(q)$ and $\omega^{\mathrm{T}}_{NN}(q)$ have only one branch which virtually coincides with the high frequency $\omega^{\mathrm{T}}_{CC}(q)$ and they take a finite value as $q \to 0$, which signals the absence of propagating shear modes. $\omega^{\mathrm{T}}_{CC}(q)$ always has one branch

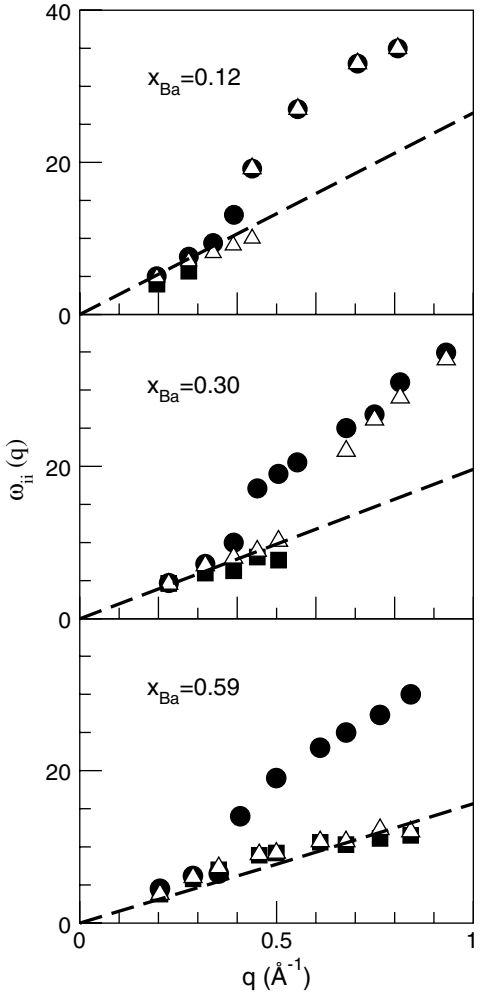

Figure 14. The dispersion relation of the collective modes in the partials, $S_{\mathrm{LiLi}}(q,\omega)$, $S_{\mathrm{BaBa}}(q,\omega)$ and $S_{NN}(q,\omega)$ (full circles, full squares and open triangles respectively), for the liquid Li–Ba alloy at several concentrations. The slope of the dashed lines shows the respective experimental adiabatic sound velocities.

connected with the minority component, whereas at $x_{\mathrm{Ba}} = 0.12, 0.30$ a second branch appears. Moreover, the low frequency $\omega^{\mathrm{T}}_{CC}(q)$ branch starts well outside the linear region and this suppression of the CC modes in the long wavelength limit is predicted by the GCM model [10] for those systems with a high mutual diffusion and a tendency towards homocoordination. We recall that the previous structural results suggested a mild homocoordination tendency at both concentrations.

In fact, the basic difference from the (longitudinal and transverse) dispersion relations of the liquid Li–Mg alloy is quantitative and stems from the greater atomic mass difference between the Li and Ba ions. It shows up in a wider gap between the $\omega^{\mathrm{L,T}}_{\mathrm{BaBa}}(q)$ and the high frequency $\omega^{\mathrm{L,T}}_{\mathrm{LiLi}}(q)$ curves as well as in the fact that the collective motions (acoustic and shear waves) are progressively hindered with increasing atomic mass mismatch.

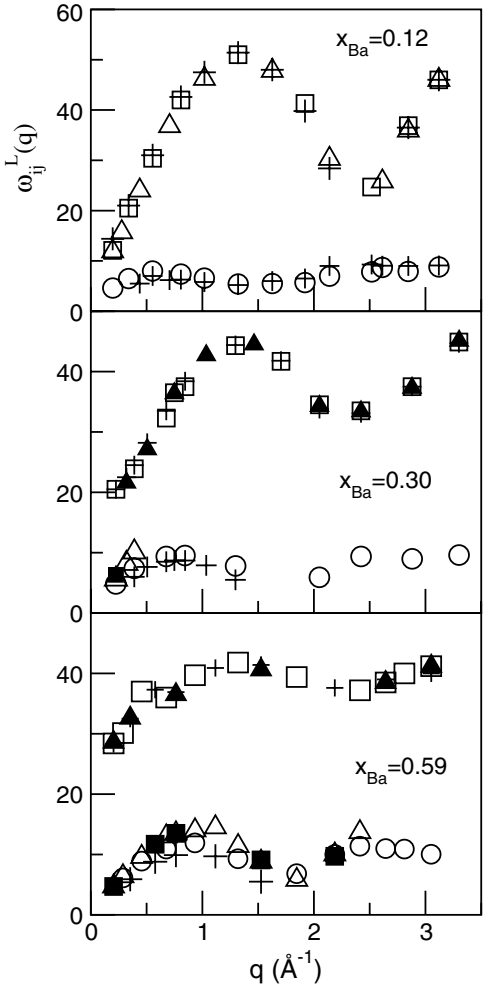

Figure 15. The longitudinal dispersion relation of the partials, $\omega^{\mathrm{L}}_{\mathrm{LiLi}}(q)$ (open squares), $\omega^{\mathrm{L}}_{\mathrm{BaBa}}(q)$ (open circles), number–number, $\omega^{\mathrm{L}}_{NN}(q)$ (open triangles) and concentration–concentration, $\omega^{\mathrm{L}}_{CC}(q)$ (plus signs) longitudinal modes, for the Li–Ba liquid alloy at the three concentrations and temperatures considered in this work.

Table 8. Calculated values of the shear viscosity η (in GPa ps) for the Li–Ba liquid alloy at $T = 575$ K ($x_{\mathrm{Ba}} = 0.12$, 0.30) and 775 K ($x_{\mathrm{Ba}} = 0.59$).

x_{Ba}	η_{Th}
0.12	0.60 ± 0.05
0.30	1.40 ± 0.1
0.59	1.65 ± 0.1

From the total transverse current correlation function and using the formalism outlined in section 3.2, we have calculated the alloy shear viscosity, η, whose values are shown in table 8. No experimental data are available for the alloy shear viscosities, but the calculated OF-AIMD value for pure Ba near the triple point is $\eta_{\mathrm{Ba}} = 2.2 \pm 0.2$ whereas its reported experimental

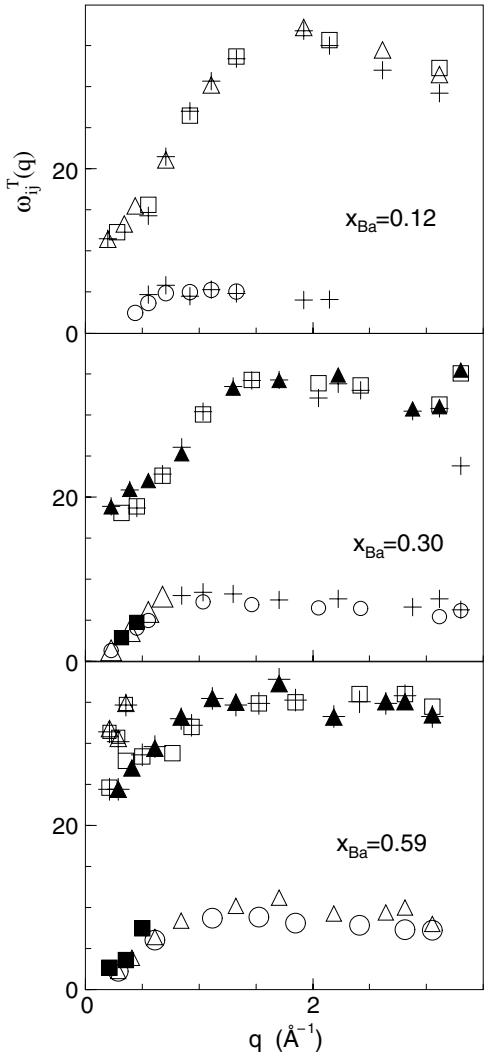

Figure 16. The transverse dispersion relation of the partials, $\omega^{\mathrm{T}}_{\mathrm{LiLi}}(q)$ (open and full squares), $\omega^{\mathrm{T}}_{\mathrm{BaBa}}(q)$ (open circles), number–number, $\omega^{\mathrm{T}}_{NN}(q)$ (open and full triangles) and concentration–concentration, $\omega^{\mathrm{T}}_{CC}(q)$ (plus signs) transverse modes, for the Li–Ba liquid alloy at the concentrations and temperatures considered in this work.

value is (in GPa ps) $\eta^{\mathrm{exp}}_{\mathrm{Ba}} = 1.82$ [56]. Using the calculated OF-AIMD value for pure Li at 575 K, namely $\eta_{\mathrm{Li}} = 0.42 \pm 0.05$, the present results for the alloy suggest some negative deviation from the linear law at $x_{\mathrm{Ba}} = 0.12$, which conforms with the mild homocoordination tendencies exhibited at this concentration [21].

5. Conclusions

We have calculated several static and dynamic properties of the liquid Li–Mg and Li–Ba alloys at different concentrations. The simulations have been performed using the orbital free *ab initio* molecular dynamics method combined with local pseudopotentials derived within the same

framework. Former calculations on pure liquid Li, Mg and Ba at their respective triple points yielded a good description of several static and dynamic properties which has prompted its application to the study of the static and dynamic properties of their binary alloys.

The results obtained for the static structural properties, as embodied by the $S_{\mathrm{T}}(q)$, provide a reasonable description of the available experimental data. The discrepancies observed in the Li–Ba alloy may be traced back to the local pseudopotential used for Ba; in fact we already noted that the description of pure liquid Ba was less accurate than those of pure liquid Li and Mg.

As for the dynamical properties, we have analysed several time correlation functions although comparison with experiment could only be made at the level of some transport coefficients. But even in this case, experimental data were normally available for the pure components and, therefore, the reliability of the results obtained for the alloys had to be substantiated in a qualitative way by connection with the known ordering tendencies in the alloy. In fact, experimental data were available only for the adiabatic velocity of sound in the liquid Li–Ba alloy and they were accurately reproduced by the present calculations.

For both alloys, the calculated partial dynamic structure factors, $S_{\mathrm{LiLi}}(q,\omega)$, $S_{\mathrm{MgMg}}(q,\omega)$ and $S_{\mathrm{BaBa}}(q,\omega)$, show clear side peaks which extend far beyond the hydrodynamic regime and represent two non-hydrodynamic modes known as the fast and slow sound modes, respectively. This phenomenon had already been predicted by the RET when applied to a binary mixture of hard spheres [8]. At that time, it was also concluded that a mass ratio larger than 10 would be required in order to expose the non-hydrodynamic modes. But the present calculations, along with previous ones on the liquid Li–Na alloy [11], have shown that those modes may also appear in systems with a significantly smaller mass ratio, $\approx$3. Furthermore, we obtain that as the wavevector q is decreased towards the hydrodynamic region, the fast sound mode smoothly merges into the hydrodynamic sound mode and this process takes place over a range of q values which becomes smaller as the mass ratio increases. In this way, whereas for the Li–Mg alloy it occurs at around $0.2\ \text{Å}^{-1} \leqslant q \leqslant 0.4\ \text{Å}^{-1}$, for the Li–Ba alloy the range moves towards smaller values, which in the $\mathrm{Li}_{0.88}\mathrm{Ba}_{0.12}$ alloy happens at $q \leqslant 0.2\ \text{Å}^{-1}$.

An interesting feature is the appearance of two branches for $\omega_{NN}^{\mathrm{L,T}}(q)$, $\omega_{\mathrm{AA}}^{\mathrm{L,T}}(q)$ (A = lighter element) and $\omega_{CC}^{\mathrm{T}}(q)$, in both the longitudinal and transverse dispersion relations, with the high frequency branches representing kinetic modes which are overdamped.

The low frequency $\omega_{NN}^{\mathrm{L}}(q)$ and $\omega_{\mathrm{AA}}^{\mathrm{L}}(q)$, along with the $\omega_{\mathrm{HH}}^{\mathrm{L}}(q)$, (H = heavier element) go linearly to zero at $q = 0$ and they represent acoustic modes. On the other hand, the low frequency $\omega_{NN}^{\mathrm{T}}(q)$ and $\omega_{\mathrm{AA}}^{\mathrm{T}}(q)$, along with the $\omega_{\mathrm{HH}}^{\mathrm{T}}(q)$, go linearly to zero at a finite q value, q_{c}, and they represent propagating shear modes. However, the low frequency $\omega_{CC}^{\mathrm{T}}(q)$ branch does not exist for low q values, as it appears just outside the linear region; this behaviour is consistent with the predictions of the GCM model. Moreover, we find that by increasing the concentration of the lighter component, the range of the low frequency $\omega_{NN}^{\mathrm{T}}(q)$ branch is diminished.

The shear viscosity of the alloy has been evaluated by means of its connection with the hydrodynamic limit of the total transverse current correlation function. The reasonable agreement with experiment of the calculated shear viscosity coefficients for the pure components provides confidence in the results obtained for the alloys. Moreover, its variation with concentration qualitatively correlates with the known ordering tendencies of both alloys.

We end up by signalling that the two main approximations in the present orbital free *ab initio* molecular dynamics method are the electronic kinetic energy functional and the local pseudopotentials describing the electron–ion interactions. Therefore, further improvements of the method will necessarily focus on developing more accurate kinetic energy functionals and local ionic pseudopotentials.

Acknowledgments

This work has been supported by the Junta de Castilla y León (VA073-02) and the DGICYT (MAT2002-04393-C0201). DJG gratefully acknowledges the financial support of the Ministry of Education, Culture and Sports of Spain and the Physics Department of Queen's University. MJS acknowledges the support of the NSERC of Canada.

References

[1] Hohenberg P and Kohn W 1964 *Phys. Rev.* **136** B864
[2] Kohn W and Sham L J 1965 *Phys. Rev.* **140** A1133
[3] Shimojo F, Zempo Y, Hoshino K and Watabe M 1996 *J. Non-Cryst. Solids* **205–207** 983
Costa-Cabral B J and Martins J L 1995 *Phys. Rev.* B **51** 872
[4] Kresse G 1996 *J. Non-Cryst. Solids* **205–207** 833
Kresse G and Hafner J 1997 *Phys. Rev.* B **55** 7539
[5] Senda Y, Shimojo F and Hoshino K 1998 *J. Phys. Soc. Japan* **67** 2753
[6] Jacucci G and McDonald I R 1980 *J. Phys. F: Met. Phys.* **10** L15
[7] Jacucci G, Ronchetti M and Schirmacher W 1984 *J. Physique Coll.* **8** C8 385
[8] Campa A and Cohen E G D 1990 *Phys. Rev.* A **41** 5451
[9] Westerhuijs P, Montfrooij W, de Graaf L A and de Schepper I M 1992 *Phys. Rev.* A **45** 3749
[10] Bryk T, Mryglog I and Kahl G 1997 *Phys. Rev.* E **56** 2903
Bryk T and Mryglod I 1999 *Phys. Lett.* A **261** 349
Bryk T and Mryglod I 2000 *J. Phys.: Condens. Matter* **12** 6063
[11] Blanco J, González D J, González L E, López J M and Stott M J 2003 *Phys. Rev.* B **67** 041204
[12] González D J, González L E, López J M and Stott M J 2003 *Europhys. Lett.* **62** 42
[13] González D J, González L E, López J M and Stott M J 2004 *Phys. Rev.* E **69** 031205
[14] Enciso E, Almarza N G, Dominguez P and Bermejo F J 1995 *Phys. Rev. Lett.* **74** 4233
[15] Crevecoeur R M, Smorenburg H E and de Schepper I M 1996 *J. Low Temp. Phys.* **105** 149
[16] Fernandez-Perea R, Alvarez M, Bermejo F J, Verkerk P, Roessli B and Enciso E 1998 *Phys. Rev.* E **58** 4568
[17] Montfrooij W, Westerhuijs P, de Haan V O and de Schepper I M 1989 *Phys. Rev. Lett.* **63** 544
[18] de Jong P H K, Verkerk P, de Vroege C F, de Graaf L A, Howells W S and Bennington S M 1994 *J. Phys.: Condens. Matter* **6** L681
[19] Alvarez M, Bermejo F J, Verkerk P and Roessli B 1998 *Phys. Rev. Lett.* **80** 2141
[20] Ruppersberg H, Saar J, Speicher W and Heitjans P 1980 *J. Physique Coll.* **41** C8 595
Chieux P and Ruppersberg H 1980 *J. Physique Coll.* **41** C8 145
[21] Ruppersberg H 1987 *Phys. Chem. Liq.* **17** 73
[22] Perrot F 1994 *J. Phys.: Condens. Matter* **6** 431
Smargiassi E and Madden P A 1994 *Phys. Rev.* B **49** 5220
Foley M and Madden P A 1996 *Phys. Rev.* B **53** 10589
[23] Garcia González P, Alvarellos J E and Chacón E 1996 *Phys. Rev.* A **54** 1897
Garcia González P, Alvarellos J E and Chacón E 1996 *Phys. Rev.* B **53** 9509
Garcia González P, Alvarellos J E and Chacón E 1998 *Phys. Rev.* B **57** 4857
[24] González D J, González L E, López J M and Stott M J 2002 *Phys. Rev.* B **65** 184201
[25] Beauchamp P, Taylor R and Vitek V 1975 *J. Phys. F: Met. Phys.* **5** 2017
[26] Dagens L, Rasolt M and Taylor R 1975 *Phys. Rev.* B **11** 2726
[27] Hafner J 1976 *J. Phys. F: Met. Phys.* **6** 1243
[28] Hafner J 1977 *Phys. Rev.* A **16** 351
[29] Harrison W A 1966 *Pseudopotentials in the Theory of Metals* (New York: Benjamin)
[30] Canales M, Gonzalez D J, Gonzalez L E and Padro J A 1998 *Phys. Rev.* E **58** 4747
[31] Anento N and Padró J A 2000 *Phys. Rev.* B **62** 11428
Anento N and Padró J A 2002 *J. Chem. Phys.* **116** 6159
[32] Anento N and Padró J A 2001 *Mol. Phys.* **99** 275
[33] Anento N, Gonzalez L E, Gonzalez D J, Chushak Y and Baumketner A 2004 *Phys. Rev.* E **40** 041201
[34] Hafner J, Pasturel A and Hicter P 1984 *J. Phys. F: Met. Phys.* **14** 1137
[35] González L E, González D J and López J M 2001 *J. Phys.: Condens. Matter* **13** 7801
González D J, González L E, López J M and Stott M J 2002 *J. Non-Cryst. Solids* **312–314** 110
[36] Waseda Y 1980 *The Structure of Non-Crystalline Materials* (New York: McGraw-Hill)

[37] Bhatia A B and Thornton D E 1970 *Phys. Rev.* B **2** 3004
[38] Warren B E 1969 *X-Ray Diffraction* (Reading, MA: Addison-Wesley)
Cowley J M 1950 *Phys. Rev.* **77** 667
Singh R N and Sommer F 1997 *Rep. Prog. Phys.* **60** 57
[39] McGreevy R L, Baranyai A and Ruff I 1986 *Phys. Chem. Liq.* **16** 47
[40] Nakanishi K, Okazaki S, Ikari K, Iguchi T and Tanaka H 1982 *J. Chem. Phys.* **76** 629
Schoen M and Hoheisel C 1984 *Mol. Phys.* **53** 1367
Borgelt P, Hoheisel C and Stell G 1990 *J. Chem. Phys.* **92** 6161
Rey C, Gallego L J, González L E and González D J 1992 *J. Chem. Phys.* **97** 5121
Abramo M C, Cacamo C and Giunta G 1986 *Phys. Rev.* A **34** 3279
[41] Trullás J and Padró J A 1993 *J. Chem. Phys.* **99** 3983
Trullás J and Padró J A 1994 *Phys. Rev.* E **50** 1162
[42] Kato T 1985 *J. Phys. Chem.* **89** 5750
[43] de Jong P H K 1993 *PhD Thesis* Technische Universiteit Delft
Feinauer A, Majer G and Seeger A 1994 *J. Phys.: Condens. Matter* **6** L355
[44] Iida T and Guthrie R I L 1988 *The Physical Properties of Liquid Metals* (Oxford: Clarendon)
[45] Darken L S and Gurry R W 1953 *Physical Chemistry of Metals* (New York: McGraw-Hill)
[46] March N H and Tosi M P 1991 *Atomic Dynamics in Liquids* (New York: Dover)
[47] Hornung K 1985 *Handbook of Thermodynamic and Transport Properties of Alkali Metals* ed R W Ohse (Oxford: Blackwell) chapter 6.4
[48] Adams E M, McDonald O R and Singer K 1977 *Proc. R. Soc.* A **357** 37
[49] Balucani U and Zoppi M 1994 *Dynamics of the Liquid State* (Oxford: Clarendon)
Hansen J P and McDonald I R 1986 *Theory of Simple Liquids* (London: Academic)
Boon J P and Yip S 1980 *Molecular Hydrodynamics* (New York: McGraw-Hill)
[50] Keller D V, Kanda F A and King A J 1958 *J. Phys. Chem.* **62** 732
[51] Saar J and Ruppersberg H 1987 *Phys. Chem. Liq.* **17** 45
[52] Gonzalez L E, Dalgıç S, Gonzalez D J and Silbert M 1996 *J. Non-Cryst. Solids* **205–207** 901
[53] Gonzalez D J, Gonzalez L E, Silbert M and Alonso J A 1993 *J. Phys.: Condens. Matter* **5** 4283
[54] Mori H, Hoshino K and Watabe M 1991 *J. Phys.: Condens. Matter* **3** 9791
[55] Alemany M M G, Casas J, Rey C, Gonzalez L E and Gallego L J 1997 *Phys. Rev.* E **56** 6818
[56] Shimoji M and Itami I 1986 *Atomic Transport in Liquid Metals* (Aedermannsdorf: Trans. Tech.)